Physics of Fluids ARTICLE pubs.aip.org/aip/pof

On the motion of hairpin filaments in the atmospheric boundary layer

Cite as: Phys. Fluids **35**, 076603 (2023); doi: 10.1063/5.0151078
Submitted: 18 March 2023 · Accepted: 19 June 2023 ·

Abhishek Harikrishnan,[1,a)] Marie Rodal,[1,2] Rupert Klein,[1] Daniel Margerit,[3] and Nikki Vercauteren[4]

AFFILIATIONS

[1]Institute of Mathematics, Freie Universität Berlin, 14195 Berlin, Germany
[2]PLECO, Department of Biology, Universiteit Antwerpen, 2610 Wilrijk, Belgium
[3]Avenue des grands pins, 31660 Toulouse, France
[4]Department of Geosciences, University of Oslo, 0371 Oslo, Norway

[a)]Author to whom correspondence should be addressed: abhishek.harikrishnan@fu-berlin.de

ABSTRACT

A recent work of Harikrishnan *et al.* ["Geometry and organization of coherent structures in stably stratified atmospheric boundary layers," arXiv:2110.02253 (2021)] has revealed an abundance of hairpin-like vortex structures, oriented in a similar direction, in the turbulent patches of a stably stratified Ekman flow. In this study, hairpin-like structures are investigated by treating them as slender vortex filaments, i.e., a vortex filament whose diameter d is small when compared to its radius of curvature R. The corrected thin-tube model of Klein and Knio ["Asymptotic vorticity structure and numerical simulation of slender vortex filaments," J. Fluid Mech. **284**, 275 (1995)] is used to compute the motion of these filaments with the atmospheric boundary layer as a background flow. Our results suggest that the orientation of the hairpin filament in the spanwise direction is linked to its initial starting height under stable stratification, whereas no such dependency can be observed with the neutrally stratified background flow. An improved feature tracking scheme based on spatial overlap for tracking Q-criterion vortex structures on the direct numerical simulation data is also developed. It overcomes the limitation of using a constant threshold in time by dynamically adjusting the thresholds to accommodate the growth or deterioration of a feature. A comparison between the feature tracking and the filament simulation reveals qualitatively similar temporal developments. Finally, an extension of the asymptotic analysis of Callegari and Ting ["Motion of a curved vortex filament with decaying vortical core and axial velocity," J. Appl. Math. **35**, 148–175 (1978)] is carried out to include the effect of gravity. The results show that, in the regime considered here, a contribution from the gravity term occurs only when the tail of an infinitely long filament is tilted at an angle relative to the wall.

I. BACKGROUND AND INTRODUCTION

Understanding the dynamics of three-dimensional vortices is an essential building block to uncovering the mysteries of turbulence. In particular, vortices possessing a unique hairpin-like geometry have been experimentally observed in turbulent boundary layers through the seminal work of Head and Bandyopadhyay.[1] Since then, numerous studies[2–7] have been carried out corroborating the existence of these entities. In a recent work, Harikrishnan *et al.*[8] analyzed the direct numerical simulations (DNS) of stratified Ekman flows,[9–11] which are simplified representations of the atmospheric boundary layer (ABL). Under very stable conditions, the flow is globally intermittent, i.e., non-turbulent flow regions on scales larger than the coherent motions exist along with the turbulent flow regions close to the wall.[12] For such flows, the authors[8] observed an abundance of hairpin-like structures within the turbulent regions of the flow. A visualization of this case is shown in Fig. 1 for which vortices were detected utilizing the popular Q-criterion,[13] which employs the second invariant of the velocity gradient tensor $(\nabla \mathbf{v})$ to classify vortices as regions where rotation dominates over the strain, i.e.,

$$Q = \frac{1}{2}(||\Omega||^2 - ||S||^2) > 0. \qquad (1)$$

In the above equation, $\Omega = \frac{1}{2}[\nabla \mathbf{v} - (\nabla \mathbf{v})^T]$ is the vorticity or spin tensor, $S = \frac{1}{2}[\nabla \mathbf{v} + (\nabla \mathbf{v})^T]$ is the strain-rate tensor, and $|| \cdot ||$ is the Euclidean norm.

For the same case visualized in Fig. 1, the poster of Harikrishnan *et al.*[14] showed that if two hairpin-like vortices are extracted randomly from different regions of the flow, the heads of the hairpin-like

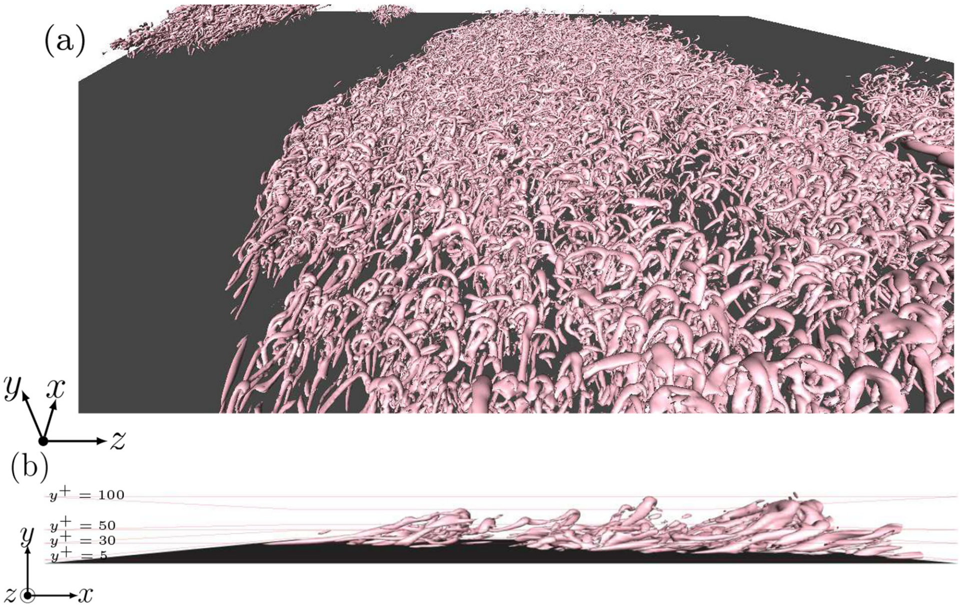

FIG. 1. (a) Hairpin-like vortex structures are visualized based on the *Q*-criterion for the strongly intermittent case (Reynolds number $= 26\,450$, and bulk Richardson number $Ri_B = 2.64$) of Harikrishnan *et al.*[8] Details of the DNS simulation are described in Sec. IV A. The visualization is shown for 1/3 of the computational domain and restricted to a wall-normal height of $y^+ = 250$ where the majority of the hairpin-like structures are visible. Regions with no vortex activity correspond to the non-turbulent/inactive regions of the flow. (b) Side view (x, y) of a hairpin packet is visualized for the same case. (x, y, z) denote the streamwise, wall-normal, and spanwise coordinates, respectively.

structures appear to be oriented in a similar direction. In a subsequent poster,[15] the Lagrangian finite-time Lyapunov exponent (FTLE) also yielded comparable results. While the *Q*-criterion is an Eulerian pointwise characterization of an instantaneous velocity field, FTLE follows fluid particle trajectories to identify regions of maximum material stretching. Initializing and advecting tracers in forward-time yields repelling Lagrangian coherent structures,[16] which have been visualized in the poster of Harikrishnan *et al.*[15] These results suggest that hairpin-like structures oriented in similar directions can be identified using both Eulerian and Lagrangian criteria under very stable conditions of the ABL.

The identification of hairpin-like structures in the ABL is not new and has been reported in previous works for various stability conditions. For instance, Hommema and Adrian[17] used smoke visualization in their field experiments to identify ramp-like structures (which are conjectured to be hairpin packets) in the first 3 m of the ABL under moderately unstable (convective) and neutral conditions. Li and Bou-Zeid[18] found signatures of hairpin vortices under neutral conditions and observed that they change to thermal plumes under highly unstable conditions. Signatures of hairpin vortices in neutral to weakly stable conditions were reported by Heisel *et al.*[19] and Lee *et al.*[20] Under stable (nocturnal) conditions, Oncley *et al.*[21] noted the presence of counter-rotating vortices, which can be interpreted as legs of hairpin vortex structures. By studying the DNS of a stably stratified shear layer akin to those observed in the atmosphere, Watanabe *et al.*[22] not only found a large number of hairpin vortices, but noted that they tend to be oriented toward the streamwise and spanwise direction in the middle and top of the shear layer, respectively.

The motion and behavior of hairpin vortices has been well documented in unstratified fluid flows. By periodically injecting fluid in a subcritical laminar boundary layer, Acarlar and Smith[2] artificially created a low-speed region resembling the low-speed streaks, first experimentally observed by Kline *et al.*[23] They noted that these regions became unstable and initiated an oscillation, which grew to form hairpin vortices. The heads of the vortices, which lift up due to self-induction, were then found to be stretched by the wall shear layer as they were carried downstream. With the linear stochastic estimation procedure, Zhou *et al.*[7] were able to isolate and study the evolution of a hairpin structure in the DNS of channel flow. They found that the circulation strength relative to the mean shear can impact the streamwise length of the hairpin vortex, with lower circulation hairpins having longer legs due to the dominance of the mean shear over self-induction. In an experimental study, Adrian *et al.*[4] observed that the inclination angle (denoted by γ), i.e., the angle of head of the hairpin with respect to the wall, is a function of its location. Near vertical orientation was observed in the outer layer, and about $20^\circ - 45^\circ$ inclination was found close to the wall. Furthermore, as the hairpin ages over time, Head and Bandyopadhyay[1] and Adrian *et al.*[4] have shown that the hairpins exhibit a characteristic growth angle, which ranges between 12° and 20°. While these studies give a good picture of the behavior of hairpin vortices in non-stratified turbulent boundary layers, their motion in stratified flows remains unexplored. Here, we would like to specifically address the following questions in this context:

(1) Starting from an initial perturbation, how do dynamic hairpin characteristics, such as inclination angle, spanwise orientation, wall-normal stretching due to shear, streamwise, and spanwise advection, change with respect to stratification? By studying these dynamic characteristics, can the abundance and orientation of hairpin-like structures in the very stable regime of the ABL be explained?
(2) Does the location of the initial perturbation, for example, in the buffer or outer layer, have an impact on the dynamics of the hairpin structure? If so, how does it change with respect to stratification?

Owing to their abundance, understanding the dynamics of hairpins can be useful to improve parametrizations of the stable boundary layer (SBL), which still remains a challenge.[24,25] In particular, the streamwise displacement (Δx) computed from the inclination angle γ of inclined features has been used to improve the wall models of large eddy simulations (LES).[26,27] This motivates the need to study the dynamics of these structures in response to changes in stratification.

By tracking features with spatial overlaps in wall-bounded flows, Lozano-Durán and Jiménez[28] showed that coherent structures, such as vortices, or quadrant structures, such as sweeps and ejections, may undergo numerous complex interactions during their lifetimes. While volume tracking of these structures with DNS data can be useful, interactions may complicate understanding of the dynamics of a structure. For instance, once the structure of interest splits into two, there is an ambiguity in following the "correct" structure, which is exacerbated when there are additional split or merge events during its lifetime. Furthermore, as the method relies on thresholding of scalar fields, it implies that some useful features of the structure may not be adequately captured (see the discussion in Sec. IV B). Hence, in this paper, we turn toward a more fundamental approach, similar to the work of Hon and Walker,[29] where hairpins are treated as vortex filaments.

In his review paper, Leonard[30] identified two methods to compute the motion of vortex filaments, namely, the thin-filament and the local induction approximations (LIA). The former is based on the slender vortex theory[31] and on related numerical methods,[32] which assume the vorticity to be highly concentrated along a "filament centerline" $\mathscr{L}(t) : s \to \mathbf{X}(s,t)$. An individual vortex core has an averaged diameter d and a characteristic radius of curvature R such that the dimensionless core size parameter δ satisfies

$$\delta = \frac{d}{R} \ll 1. \tag{2}$$

In an unbounded domain, the velocity induced by this filament at a point $\mathbf{P}$ and time t in a three-dimensional inviscid and irrotational flow field in the outer flow region, i.e., away from the vortical core, is given by the line-Biot–Savart law as[31]

$$\mathbf{Q}_1(\mathbf{P},t) = -\frac{\Gamma}{4\pi}\int_{\mathscr{L}} \frac{\big(\mathbf{P}-\mathbf{X}(s',t)\big)\times \mathbf{ds}'}{|\mathbf{P}-\mathbf{X}(s',t)|^3}, \tag{3}$$

where Γ is the circulation of the filament. As $\mathbf{P}$ moves toward the filament centerline, $\mathbf{Q}_1(\mathbf{P},t)$ becomes singular, and thus the line Biot–Savart integral cannot alone predict the self-induced vortex motion. With matched asymptotic expansions, Callegari and Ting[31] showed how this singularity is naturally regularized within the framework of the Navier–Stokes equations, and they provided explicit expressions for the velocity of points on the filament centerline for a closed filament. Adapting this for a non-closed, infinite filament leads to the following equation:

$$\frac{\partial}{\partial t}\mathbf{X}(s,t) = \frac{\Gamma}{4\pi}\kappa\mathbf{b}(s,t)\left(\ln\left(\frac{2}{\delta}\right) + C(t)\right) + \mathbf{Q}_0(s,t), \tag{4}$$

where

$$\mathbf{Q}_0(s,t) = \mathbf{Q}_\mathrm{f}(s,t) + \mathbf{Q}_2(\mathbf{X}(s,t)) \tag{5}$$

is the superposition of the nonsingular remainder of the line-Biot–Savart integral $\mathbf{Q}_f$, and of a superimposed background flow $\mathbf{Q}_2$ (taken on the filament), such as the shear flow in a boundary layer. The other method named LIA (for "local induction approximation") is a simplification of the thin-filament approximation,[33] in which the long-distance induction effects represented by $\mathbf{Q}_0(s,t)$ and the local effects from the core vorticity distribution represented by $C(t)$ in Eq. (4) are neglected, so that the filament motion is due to the curvature/binormal term alone. In this paper, it is used mainly for validation purposes and the effect of omission of long-distance effects is exemplified in Sec. III. Therefore, hairpin evolution is simulated using the slender filament approach, implemented numerically by the corrected thin-tube model of Klein and Knio.[32] In this context, in addition to the previous research questions, we also address the following one:

(3) Can a suitable tracking methodology based on volume or spatial overlap be developed that respects the dynamical evolution of features in time? Qualitatively, how much would the results differ with those obtained through simulation with the Biot–Savart law?

Finally, the influence of gravity on the self-induced motion of the slender vortex filament is explored. An asymptotic analysis extending the work of Callegari and Ting[31] is carried out to include the effect of gravity and is presented in Sec. VI. To the author's knowledge, the only attempt at including the effect of gravity in the filament motion equations was presented by Chang and Smith.[34] They extended the force balance method of Moore and Saffman[35] to include the force of gravity, but assumed the fluid density in the *a priori* assigned core of the filament to be constant, so that a self-consistent evolution of the fluid density was not considered. They used this to demonstrate that buoyant vortex rings expand as they rise, as has indeed been observed experimentally by Turner.[36] In our work, we will account for the fact that the dominant reason for density variations in the ABL is the transport of air from different heights in the boundary layer, but that there is no diabatic effect, such as combustion, that would specifically affect the vortex core temperature and density. Hence, we assume that the influence of gravity on the core flow is weak, but that it may have a stronger influence on the external flow. For simplicity, we will refrain from doing the full compressible flow analysis, as was done by Ting *et al.*[37] and Knio *et al.*,[38] and instead employ the Boussinesq approximation so that the density perturbation only appears in the gravity term. This simplification is justified as our focus of interest is in the ABL, which to a large extent can be assumed to be incompressible. This leads us to our final research question, which is given as follows:

(4) What effect does gravity have on the fluid flow within the vortex filament and hence on the self-induced motion of the filament, given the assumptions listed above?

In Sec. II, the initial configuration of the hairpin filament is described, along with both numerical methods considered in this paper, which are the local induction approximation (LIA) and the corrected thin-tube model of Klein and Knio,[32] henceforth denoted M1 KK. Here, M1 refers to the method 1 optimization technique of Knio and Klein.[39] The results of the filament simulation are discussed in Secs. III and IV. In the former, comparisons are made between the temporal evolution of hairpin filament with LIA and M1 KK methods, which highlight the drawback of LIA owing to its neglect of nonlocal effects. In the latter, the evolution of hairpin filaments when subjected to a mean background flow obtained from stratified Ekman flow simulations of Ansorge[11] is studied under different degrees of stratification. A comparison is also made between the filament simulation and tracking of a Q-criterion structure in the DNS data with a feature tracking scheme in Sec. V. Since our implementations of the thin-tube filament numerics do not account for the effect of gravity on the self-induced motion of the vortex, a theoretical justification via matched asymptotics in the regime of weak density variations is carried out in Sec. VI. Our conclusions are presented in Sec. VII.

II. NUMERICAL METHODS

For all simulations in this work, the initial configuration of the hairpin is chosen as a small, symmetrical, three-dimensional perturbation as seen in the work of Hon and Walker,[40] which is given by

$$\mathbf{X}(s,t) = A\left[(\cos\gamma)\hat{\mathbf{i}} + (\sin\gamma)\hat{\mathbf{j}}\right]e^{-\beta s^2} + \hat{\mathbf{j}} + s\hat{\mathbf{k}}, \tag{6}$$

where $(\hat{\mathbf{i}}, \hat{\mathbf{j}}, \hat{\mathbf{k}})$ denote the unit vectors along the streamwise (x), wall-normal (y), and spanwise (z) directions, respectively, and s is an arc length parameter along the filament. The perturbation is symmetric around $s = 0$ with an amplitude A and tilted at an angle γ with respect to the wall as sketched in Fig. 2. The parameter β is simply a large number, which controls the initial width of the perturbation.

As stated in the introduction, two methods are implemented to simulate the motion of the centerline, namely (a straightforward discretization of), the LIA and the corrected thin-tube model of Klein and Knio[32]

A. Local induction approximation

Since local induction approximation (LIA) has been discussed extensively in previous works,[41–44] only a brief overview is presented here. LIA neglects both the long-distance induction effects, $\mathbf{Q}_0(s,t)$, and the local effects from the core vorticity distribution, $C(t)$. It assumes a small core radius such that the only contribution to the motion of the filament is due to its curvature. This leads to a simplified equation of motion, which is written as

$$\frac{\partial}{\partial t}\mathbf{X}(s,t) = \frac{\Gamma}{4\pi}\kappa\mathbf{b}(s,t)\ln\left(\frac{2}{\delta}\right), \tag{7}$$

where $\kappa\mathbf{b}(s,t)$ is the curvature in the binormal direction. Klein and Majda[45,46] note that this binormal term alone cannot account for the self-stretching of vortex filaments, which is due entirely to nonlocal induction. Therefore, LIA is used only for validation purposes in this paper. In order to make the results of LIA comparable to the corrected thin-tube model presented in Sec. II B, we follow the work of Margerit *et al.*[43] who used the Callegari and Ting equation[31] without the nonlocal self-induction term $\mathbf{Q}_0(s,t)$. For a non-closed, infinite filament, the equation of motion is written as follows:

$$\frac{\partial}{\partial t}\mathbf{X}(s,t) = \frac{\Gamma}{4\pi}\kappa\mathbf{b}(s,t)\left[\ln\left(\frac{2}{\delta}\right) + C(t)\right], \tag{8}$$

where $C(t)$ is the core structure coefficient. It is natural to see this local term as an $\mathcal{O}(1)$ correction to the local induction contribution of the self-induced velocity and to call it the local induction approximation (or contribution) at $\mathcal{O}(1)$.

B. M1 corrected thin-tube model (M1 KK)

In this method, slender vortices are represented as a chain of overlapping elements satisfying the following overlap condition:

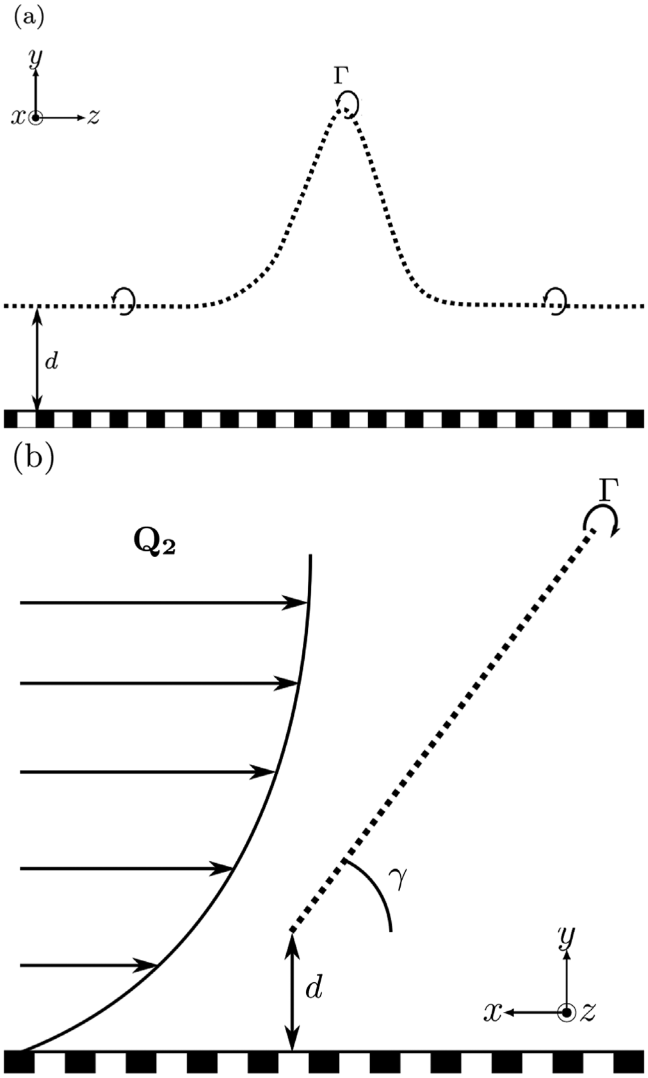

FIG. 2. (a) Illustration of hairpin shaped filament (dashed line) when viewed from the front. The filament is placed at a distance d away from the lower boundary. (b) The hairpin filament when viewed from the side including the background shear flow, $\mathbf{Q}_2$. Here, the filament can be seen tilted at an angle γ from the wall.

$$\max_{i=1..N}|\delta\boldsymbol{\chi}_i| < \delta. \tag{9}$$

Here, δ is the core radius, and $\{\boldsymbol{\chi}_i\}_{i=1}^{N}$ are N vortex elements along the filament centerline. The total vorticity experienced by the filament is given as

$$\boldsymbol{\omega}(\boldsymbol{x},t) = \sum_{i=1}^{N}\Gamma\delta\boldsymbol{\chi}_i(t)f_\delta(\boldsymbol{x} - \boldsymbol{\chi}_i^c(t)). \tag{10}$$

In this formula, Γ is a time-independent constant circulation, $\boldsymbol{\chi}_i^c(t)$ denotes the centers, and $\delta\boldsymbol{\chi}_i(t)$ the secant vectors that approximate the filament centerline and are positively aligned with the vorticity, i.e.,

$$\delta\boldsymbol{\chi}_i(t) = \boldsymbol{\chi}_{i+1}(t) - \boldsymbol{\chi}_i(t)\,, \quad \boldsymbol{\chi}_i^c(t) = \frac{\boldsymbol{\chi}_{i+1}(t) + \boldsymbol{\chi}_i(t)}{2}. \tag{11}$$

The smoothing function f_δ is related to a rapidly decaying numerical core vorticity distribution and is given by

$$f_\delta = \frac{1}{\delta^3} f\left(\frac{|\boldsymbol{x}|}{\delta}\right). \tag{12}$$

The velocity is obtained by inserting Eq. (10) in the three-dimensional Biot–Savart integral

$$\boldsymbol{v}(\boldsymbol{x}, t) = -\frac{1}{4\pi}\int\!\!\int\!\!\int \frac{\boldsymbol{x} - \boldsymbol{x}'}{|\boldsymbol{x} - \boldsymbol{x}'|^3} \times \boldsymbol{\omega}(\boldsymbol{x}')d\boldsymbol{x}', \tag{13}$$

where $d\boldsymbol{x}' = dx_1' dx_2' dx_3'$ is a volume element. The result reads

$$\boldsymbol{v}^{\mathrm{ttm}}(\boldsymbol{x}, t) = -\frac{\Gamma}{4\pi}\sum_{i=i}^{N} \frac{(\boldsymbol{x} - \boldsymbol{\chi}_i^c(t)) \times \delta\boldsymbol{\chi}_i(t)}{|\boldsymbol{x} - \boldsymbol{\chi}_i^c(t)|^3}\kappa_\delta(\boldsymbol{x} - \boldsymbol{\chi}_i^c(t)) \tag{14}$$

and $\kappa_\delta \equiv \kappa(|\boldsymbol{x}|/\delta)$ is the velocity smoothing function, which is directly related to the numerical core vorticity distribution f from Eq. (12). Equation (14) is the *standard* thin-tube model used by Chorin[47] and Knio and Ghoniem.[48] Since this model assumes that the induced velocity at the nodes by the *numerical* core vorticity distribution is the local filament velocity, it is prone to $\mathcal{O}(1)$ errors. To circumvent this, Klein and Knio[32] propose three correction strategies based on an asymptotic analysis of the numerical vorticity structure. We choose the third method due to its simplicity. This involves a rescaling of the numerical core radius as follows:

$$\delta^{\mathrm{ttm}} = \delta\, \exp\left(C^{\mathrm{ttm}} - C\right). \tag{15}$$

Here, C^{ttm} is the numerical core constant. If we choose the velocity core smoothing function $\kappa(r) = \tanh(r^3)$, then $C^{\mathrm{ttm}} = -0.4202$ as obtained by Knio and Klein.[39] According to the asymptotic theory, the core structure coefficient C includes contributions from the local swirling and axial velocities, denoted by C_v and C_w, respectively,

$$C = -1 + C_v + C_w. \tag{16}$$

Depending on the presence/absence of viscous effects and the initial leading-order velocity profile in the core, different expressions of the core structure coefficients can be obtained. Following Ting and Klein[49] for the case of a similar vortex core with the same initial core size and circulation without axial flow, C_v and C_w are given by

$$C_v = \frac{1 + \gamma_E - \ln(2)}{2} - \ln(\bar{\delta}), \tag{17}$$

$$C_w = -2\left[\frac{m(0)}{\Gamma\bar{\delta}}\right]^2\left[\frac{S_0}{S(t)}\right]^4, \tag{18}$$

where S_0 is the initial length of the filament, $\bar{\delta}$ is the stretched radius whose exact formula is given in Ting and Klein,[49] $m(0)$ is the initial axial flux of the vortex, and $\gamma_E = 0.577$ is Euler's constant. In our case, $m(0) = 0$ implying no contribution from axial velocity. We remark that (16) is usually written as $C = C_v + C_w$ [for instance, see Eq. (2) of Ref. 39]. The inclusion of -1 accounts for the difference in the definition of C_v [compare Eq. (2.3.73e) of Ref. 49 and Eq. (3) of Ref. 39].

Boundary conditions: For hairpin filaments that are periodic in the spanwise direction and embedded in an unbounded domain in the other two directions, the total velocity $\boldsymbol{v}^{\mathrm{ttm}}$ requires contributions from an infinite number of images in addition to the elements within the computational domain[50] Therefore, Eq. (14) is written as

$$\boldsymbol{v}^{\mathrm{ttm}}(\boldsymbol{x}, t) = -\frac{\Gamma}{4\pi}\sum_{k=\pm 1}^{\pm\infty}\sum_{i=i}^{N} \frac{(\boldsymbol{x} - \boldsymbol{\chi}_i^c(t)) \times \delta\boldsymbol{\chi}_i(t)}{|\boldsymbol{x} - \boldsymbol{\chi}_i^c(t)|^3}\kappa_\delta(\boldsymbol{x} - \boldsymbol{\chi}_i^c(t)). \tag{19}$$

To overcome the evaluation over an infinite number of images, the equation is split into two components,

$$\boldsymbol{v}^{\mathrm{ttm}}(\boldsymbol{x}) = \sum_{i=1}^{N}(\boldsymbol{v}_{\mathrm{center}}(\boldsymbol{x}) + \boldsymbol{v}_{\mathrm{image}}(\boldsymbol{x})), \tag{20}$$

where $\boldsymbol{v}_{\mathrm{center}}$ is the contribution from the central part of the domain, and $\boldsymbol{v}_{\mathrm{image}}$ from the images on the left and right side. They are computed as follows:

$$\boldsymbol{v}_{\mathrm{center}}(\boldsymbol{x}) = -\frac{\Gamma}{4\pi}\sum_{i=i}^{N} \frac{(\boldsymbol{x} - \boldsymbol{\chi}_i^c(t)) \times \delta\boldsymbol{\chi}_i(t)}{|\boldsymbol{x} - \boldsymbol{\chi}_i^c(t)|^3}\kappa_\delta(\boldsymbol{x} - \boldsymbol{\chi}_i^c(t)), \tag{21}$$

$$\boldsymbol{v}_{\mathrm{image}}(\boldsymbol{x}) = -\frac{\Gamma}{4\pi}\sum_{k=\pm 1}^{\pm P}\sum_{i=i}^{N} \frac{(\boldsymbol{x} - \boldsymbol{\chi}_i^c(t)) \times \delta\boldsymbol{\chi}_i(t)}{|\boldsymbol{x} - \boldsymbol{\chi}_i^c(t)|^3}. \tag{22}$$

For the image contribution, the effect of the velocity smoothing function is neglected due to the assumption of $L \gg \delta$ and $\pm P$ is a cutoff number chosen to represent the number of images on either side of the domain. The choice of P is explained in Appendix C.

Optimization: To compensate for the high resolution requirements for thin vortices, Knio and Klein[39] suggested three optimization techniques. The first method, henceforth referred to as M1 technique, is attractive and used in this work since it requires only minor modifications to the existing code and does not require computation of the curvature, κ. The corrected velocity is obtained through a Richardson-type extrapolation in the core size parameter as follows:

$$\mathbf{v}_{\mathrm{corr}}^{\mathrm{ttm}} = \boldsymbol{v}_1 + (\boldsymbol{v}_1 - \boldsymbol{v}_2)\frac{\ln\left(\sigma_1/\delta^{\mathrm{ttm}}\right)}{\ln\phi}, \tag{23}$$

where $\boldsymbol{v}_1$ and $\boldsymbol{v}_2$ are the velocities corresponding to two large core sizes σ_1 and σ_2. If $\sigma_0(t) = max_{i=1..N}|\delta\boldsymbol{\chi}_i|$ denotes the inter-element separation distance, then

$$\sigma_1 = K\,\sigma_0, \;\; \sigma_2 = \phi\,\sigma_1. \tag{24}$$

The constants K and ϕ are chosen as 3 and 2, respectively, and the choice of these parameters is described in Appendix C. The vortex elements move along Lagrangian trajectories with the following equation of motion:

$$\frac{d\boldsymbol{\chi}_i(t)}{dt} = \mathbf{v}_{\mathrm{corr}}^{\mathrm{ttm}}(\boldsymbol{\chi}_i(t), t). \tag{25}$$

A summary of the numerical scheme is presented as follows:

1. First, the initial configuration of the hairpin is setup.
2. For the chosen velocity core smoothing function $\kappa(r) = \tanh(r^3)$, C^{ttm} is set to -0.4202. The numerical core radius δ^{ttm} is computed from (15). With $\sigma_0(t) = max_{i=1..N}|\delta\boldsymbol{\chi}_i|$, (24) can be used to compute the two coarse radii.
3. For both core radii, (14) is evaluated at each node location by applying the periodic boundary condition as illustrated in

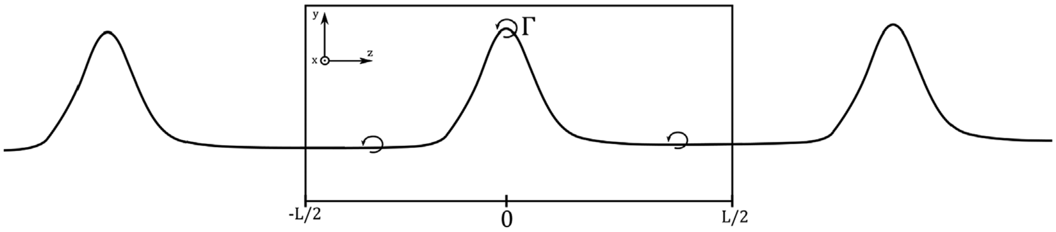

FIG. 3. Illustration of the periodic boundary conditions. A long filament periodic in the axial direction is envisioned. The domain of integration of length *L* contains one complete period.

Fig. 3, i.e., the velocity at a node x inside the computational domain is evaluated by applying a translation along the periodicity direction such that x is at the center of the domain.

(4) The corrected velocity is obtained according to Eq. (23).

(5) Finally, the node positions are updated with the equation of motion (25) with a fifth-order Adams–Bashforth scheme and Runge–Kutta–Fehlberg initialization.[51,52]

Both LIA and the M1 KK methods are written in python, and the filament code is validated against the static test of Klein and Knio,[32] which is shown in Appendix A.

III. TEMPORAL EVOLUTION OF A HAIRPIN FILAMENT IN STAGNANT BACKGROUND FLOW ($\mathbf{Q_2} = 0$)

In this section, we consider a case, in which a hairpin filament is allowed to evolve in a stagnant background flow, i.e., $\mathbf{Q}_2 = 0$ as shown in the work of Hon and Walker.[40] Both the LIA and M1 KK methods are used to compute the motion of the filament. The goal of this section is twofold: (1) This case serves as a further validation of the filament code written during the course of this work, and (2) it also highlights the differences between LIA and the M1 KK approximations. The hairpin is initially inclined at $\gamma = 45°$ with respect to the streamwise direction, having an amplitude $A = 0.5$, spread parameter $\beta = 20$, and a dimensionless core size $\delta = 0.02$. Additionally, circulation is set as $\Gamma = 1$, and a spatial discretization of 700 nodes over a length of $L = 4$ is used. In all simulations, care is taken to ensure that an adequate number of nodes are used and further refinement does not alter the results and conclusions presented in the paper.

The results of the simulation are shown in Fig. 4. For LIA, high temporal resolution is necessary to guarantee the smoothness of the filament curve required to allow for the accurate evaluation of its curvature. Accordingly, a time step of $\Delta t = 10^{-5}$ is chosen. The simulation is stopped at $t = 0.2$ when the disturbance or "wiggles" have propagated to the ends of the domain. The M1 KK scheme allows for a larger time step $\Delta t = 10^{-3}$ as it not only avoids the evaluations of local curvature κ where higher-order derivatives need to be computed,[43,48] but also is much better conditioned owing to the Richardson-type extrapolation from the artificially enlarged to the actual core size in the correction scheme M1. As for LIA, the simulation is stopped at time $t = 0.2$. The results from both panels in Fig. 4(b) show that the methods correctly capture the "corkscrew"

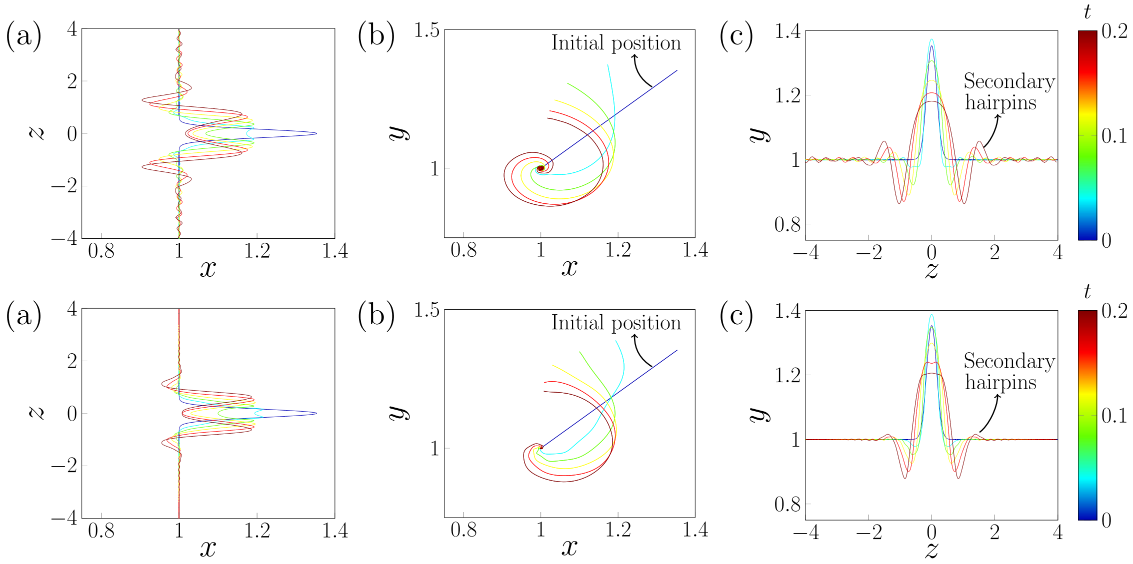

FIG. 4. Temporal evolution of a hairpin vortex in a stagnant background flow. (a)–(c) The top, side, and front view of the hairpin, respectively. The simulation performed with LIA is shown in the top panel and M1 KK method in the bottom panel.

shape described in Hon and Walker,[40] with the head of the vortex moving back and toward the wall rapidly due to self-induction in the counterclockwise direction. Other features, such as the formation of hairpin "legs" and the secondary hairpins on either side of the main disturbance, are also visible. Similar findings were also reported by Moin *et al.*,[53] who studied a parabolic vortex filament with a cutoff method. See Sec. III A of Moin *et al.*[53] for details on their setup.

Keeping everything else constant, two values of spread parameter (which controls the initial width of the perturbation) $\beta = 15, 50$ are tested. It should be noted that increasing the value of β decreases the spanwise width and vice versa. The results are shown in Fig. 5 where the simulation is stopped at $t = 0.1$ once the general trends were evident. It should be noted that the simulation for $\beta = 50$ was run with 1300 nodes and for LIA, with an even smaller time step $\Delta t = 10^{-6}$ to obtain a stable evolution. It is immediately apparent that there is a difference in the shape of the hairpin legs and how they evolve, particularly at $\beta = 50$. From the insets of Figs. 5(a)–5(d), it can be seen that by changing the spread parameter from $\beta = 15$ to $\beta = 50$, LIA effectively maintains the corkscrew spiral and at $\beta = 50$ (smaller width), there appears to be further coiling around the origin of the filament. With the M1 KK method, this corkscrew pattern cannot be seen in both cases. Further magnification near the origin of the filament as shown in Fig. 5(e) reveals only slight coiling for the M1 KK case at $t = 0.1$ for larger β. However, continuing the simulation (not shown in the paper) eventually reveals the corkscrew spiral for $\beta = 15$ as early as $t = 0.13$, while it is delayed further for $\beta = 50$ and is accompanied by further outward stretching of the hairpin legs than in the former case. This suggests that as the spanwise width of the filament is decreased, the nonlocal effects become important, which is ignored by LIA. This gives a direct comparison to the hairpin evolution under the absence of nonlocal effects with LIA where the legs of the filament do not "see" each other when they approach closely and when the nonlocal effects are correctly represented by the M1 KK method, which results in self-stretching of the filament. Therefore, all further simulations are carried out only using the M1 KK method.

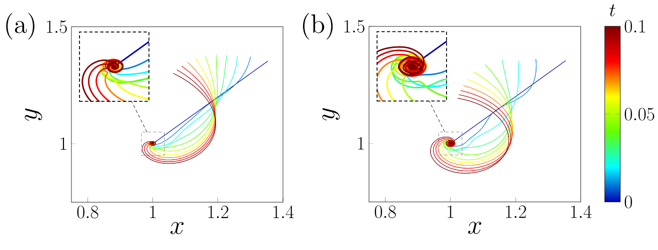

LIA with $\beta = 15$ LIA with $\beta = 50$

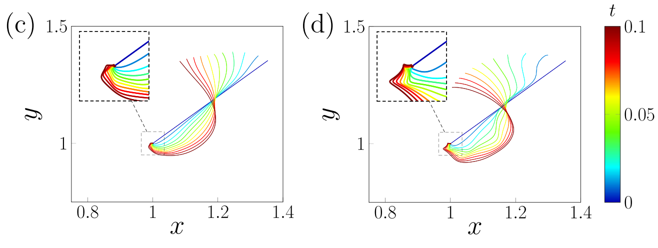

M1 KK with $\beta = 15$ M1 KK with $\beta = 50$

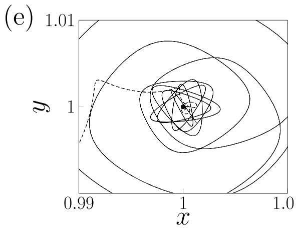

FIG. 5. The test shown in Fig. 4 is repeated with $\beta = 15, 50$ for both methods. (a) and (b) The temporal evolution of the hairpin with LIA, whereas (c) and (d) the temporal evolution with the M1 KK method. The insets in (a)–(d) show magnified portion of the filaments. Further magnified portion of the LIA (solid line) and the M1 KK (dashed line) cases with $\beta = 50$ at $t = 0.1$ is plotted in (e) with the scatter point indicating the origin of the filament.

IV. TEMPORAL EVOLUTION OF A HAIRPIN FILAMENT IN ABL BACKGROUND FLOW

The evolution of a hairpin filament immersed in an atmospheric boundary layer flow is studied here. In this section, as mentioned in the introduction, we attempt to answer our questions regarding the abundance and orientation of hairpin structures in the stably stratified ABL by studying the dynamic hairpin characteristics with respect to changes in stratification. First, the mean background flow profiles are computed from the DNS database and discussed in Sec. IV A. Then, with four initial conditions of the hairpin identified in Sec. IV B, the temporal evolution of the hairpin filament is discussed in Secs. IV C and IV D.

A. Background flow

Before the initial conditions for the hairpin simulations are discussed, a preprocessing step is carried out on the DNS database analyzed in Harikrishnan *et al.*[8] to obtain the mean background flow $\mathbf{Q_2}$. In the DNS simulation, the governing equations of an incompressible, rotating, stratified viscous fluid are solved in the Boussinesq limit where density variations are neglected except when acted upon by gravity. The simplified set of equations are[9]

$$\frac{\partial u_i}{\partial t} = -u_j\frac{\partial u_i}{\partial x_j} + \nu\frac{\partial^2 u_i}{\partial x_j^2} - \frac{\partial \pi}{\partial x_i} + f\varepsilon_{i3k}(u_k - G\delta_{k1}) + b\delta_{i3}, \quad (26a)$$

$$\frac{\partial b}{\partial t} = -u_j\frac{\partial b}{\partial x_j} + \nu_H\frac{\partial^2 b}{\partial x_j^2}, \quad (26b)$$

$$\frac{\partial u_i}{\partial x_i} = 0. \quad (26c)$$

Here, $u_{i,i\in\{1,2,3\}}$ are the velocity components, and $b = g\theta/\theta_0$ is the buoyancy, where g is the gravity, and θ, θ_0 are the potential and reference background temperatures, respectively. It should be noted that $b = 0$ under neutral stratification. $\pi = p/\rho_0$ is the pressure term with reference density ρ_0, f is the Coriolis parameter, ν_H is the diffusivity, and G is the geostrophic wind velocity magnitude. The f-plane approximation is used with $f = 2\Omega\sin\Phi\boldsymbol{e}_y$, where Ω is the Earth rotation rate, Φ is the latitude, and $\boldsymbol{e}_y$ is the vertical unit vector. This corresponds to a system, which is subjected only to a vertical rotation rate with an intensity $\Omega\sin\Phi$. The boundary conditions resemble an Ekman flow over a smooth wall with no-slip and free-slip conditions at the lower and upper boundary, respectively. The domain is doubly periodic in the horizontal directions to capture the largest relevant structures.

In the neutrally stratified case, once the flow is fully developed, it is governed by the quantities G, f, ν, and ν_H. The Coriolis parameter f is replaced by the laminar Ekman layer depth $D = \sqrt{2\nu/f}$ in the dimensional analysis. The corresponding Reynolds number is defined as $Re = GD/\nu$, and the Prandtl number $Pr = \nu/\nu_H$ is set to 1. The Ekman flow reaches steady state due to the balance of turbulence production due to shear and turbulence suppression as a result of rotation, and this steady state solution in terms of a statistical description of turbulence is a function of Re only.[10] After the flow becomes turbulent, the laminar Ekman depth D cannot be used to describe the flow and the boundary layer height under neutral conditions $\delta_h = u_\tau/f$ (determined through averages over the last inertial period) is used instead. The Reynolds number is, therefore,

$$Re = \frac{G\delta_h}{\nu}. \tag{27}$$

Here, Re = 26 450. To simulate stably stratified cases, the fully turbulent, statistically steady, and neutrally stratified flow is used as an initial condition for the velocity fields and buoyancy profile is given by an error function in the wall-normal direction [see Eq. (2.14) of Ref. 11]. For stronger stratification, cases with intermediate stratification are used as an initial condition and the buoyancy field is multiplied by some value to match the required bulk stratification. The horizontal domain size, expressed in terms of the boundary layer height under neutral conditions, is $20.4 \times 20.4\,\delta_h^2$. The strength of stratification is quantified with the dimensionless bulk Richardson number (Ri_B) defined as

$$\mathrm{Ri_B} \equiv \frac{B_0\delta_\mathrm{h}}{G^2}, \tag{28}$$

where B_0 is the difference in buoyancy between the top and bottom layer. This is related to the Froude number (Fr), another parameter for quantifying the strength of stratification, as $\mathrm{Ri_B} = \mathrm{Fr}^{-1}(\delta_\mathrm{h}/\Lambda)$, where Λ is the Rossby deformation radius. The governing equations were integrated with a high-order finite difference scheme on a structured, collocated grid composed of 3072 × 512 × 6144 points in the streamwise, wall-normal, and spanwise directions, respectively. The grid is unequally spaced in the wall-normal direction, and the top boundary is at $y = 3\delta_h$. Time integration was carried out with a fourth-order Runge–Kutta algorithm. This simulation database is ideal for our study as global intermittency is simulated without any external triggers, such as low-level jets, internal gravity waves, or surface heterogeneities.[9] Further details regarding the simulation can be found in Ansorge and Mellado[9,10] and Ansorge.[11]

In this paper, the hairpins are simulated in a mean background flow composed of two stably stratified cases (S_1, S_2) with different degrees of stratification and a neutrally stratified case (N). By studying the temporal evolution of vertically integrated turbulent kinetic energy (TKE), both S_1 and S_2 are classified under the very stable regime in which large patches of inactive/non-turbulent regions are visible. This can be seen from Figs. 6(b) and 6(c). The simulation parameters for the three cases are summarized in Table I. The streamwise (x), wall-normal (y), and spanwise (z) direction along with their corresponding velocities are represented in terms of viscous or wall units. For instance,

$$x^+ \equiv \frac{xu_\tau}{\nu}, \quad u^+ = \frac{u}{u_\tau}. \tag{29}$$

$\mathbf{Q_2}$ is obtained by computing the horizontal (x, z) mean velocity at every wall-normal height of the flow field. The mean velocity profiles are shown in Fig. 7.

B. Initial conditions

As described in Sec. II, the first step of the numerical scheme is to set up the initial configuration of the hairpin by fixing unknown physical and numerical parameters. We inspect the DNS database to inform our choice on the selection of parameters.

Three hairpin-like structures identified using the Q-criterion indicator are extracted and examined for case N, S_1, and S_2. The centerlines for the extracted structures are obtained with the blockwise skeletonization method of Fouard *et al.*[54] At each point on a centerline, the diameter d of the vortex core is estimated by fitting the largest sphere within the structure. Additionally, the radius of curvature R at every point of the parametrized centerline $\mathbf{X}$ is given by[55]

$$R = \frac{1}{\kappa} = \frac{|\mathbf{X}_s|^3}{\sqrt{|\mathbf{X}_s|^2|\mathbf{X}_{ss}|^2 - (\mathbf{X}_s \cdot \mathbf{X}_{ss})^2}}, \tag{30}$$

where $\mathbf{X}_s, \mathbf{X}_{ss}$ correspond to the first and second derivatives of the space curve along the parameterized centerline. The ratio d/R is the local dimensionless core size parameter of the filament [not to be confused with the asymptotic parameter δ from Eq. (2), which is a characteristic value of this quantity for a given filament].

Along the hairpin, the local core size parameter estimated from all hairpins and tabulated in Table II varies between 0.02 at its thinnest point up to 5.79 at its thickest. It is important to note that these estimations strongly depend on the threshold, denoted by τ, as illustrated in Fig. 8(a), where smaller thresholds imply thicker cores and vice versa. The thresholds used in this paper were obtained through the work of Harikrishnan *et al.*[8] where optimum threshold values were computed with percolation analysis. It should also be noted that these estimations are made at a later stage in the lifetime of the hairpin-like structure. Figure 8(b) shows the variations of the core size along the hairpin. For our simulations, we conservatively choose $\delta = 0.01, 0.05$ to examine the effect of changes in the core size.

For the same hairpin-like structures, circulation is computed on both legs for every wall-normal plane until the head of the structure. The estimated values are listed in Table III, which show positive values on one leg and negative values on the other indicating opposing direction of rotation. Similar to the core size, two values of circulation $\Gamma = 0.01, 0.05$ are chosen to study their impact on the evolution of hairpin.

In their experimental study, Acarlar and Smith[3] showed that low-speed momentum regions (which are also referred to as low-speed streaks) introduced in sub-critical laminar boundary layer oscillate and later break down into hairpin vortices. Therefore, the spread parameter β is chosen by computing the average spanwise width over all individual low-speed streaks at a particular height. From Fig. 1(b), numerous hairpin structures can be seen around $y^+ = 50$. Therefore, for this initial height, the mean spanwise width of the low-speed streaks is about 60 viscous units, which corresponds to $\beta = 7500$.

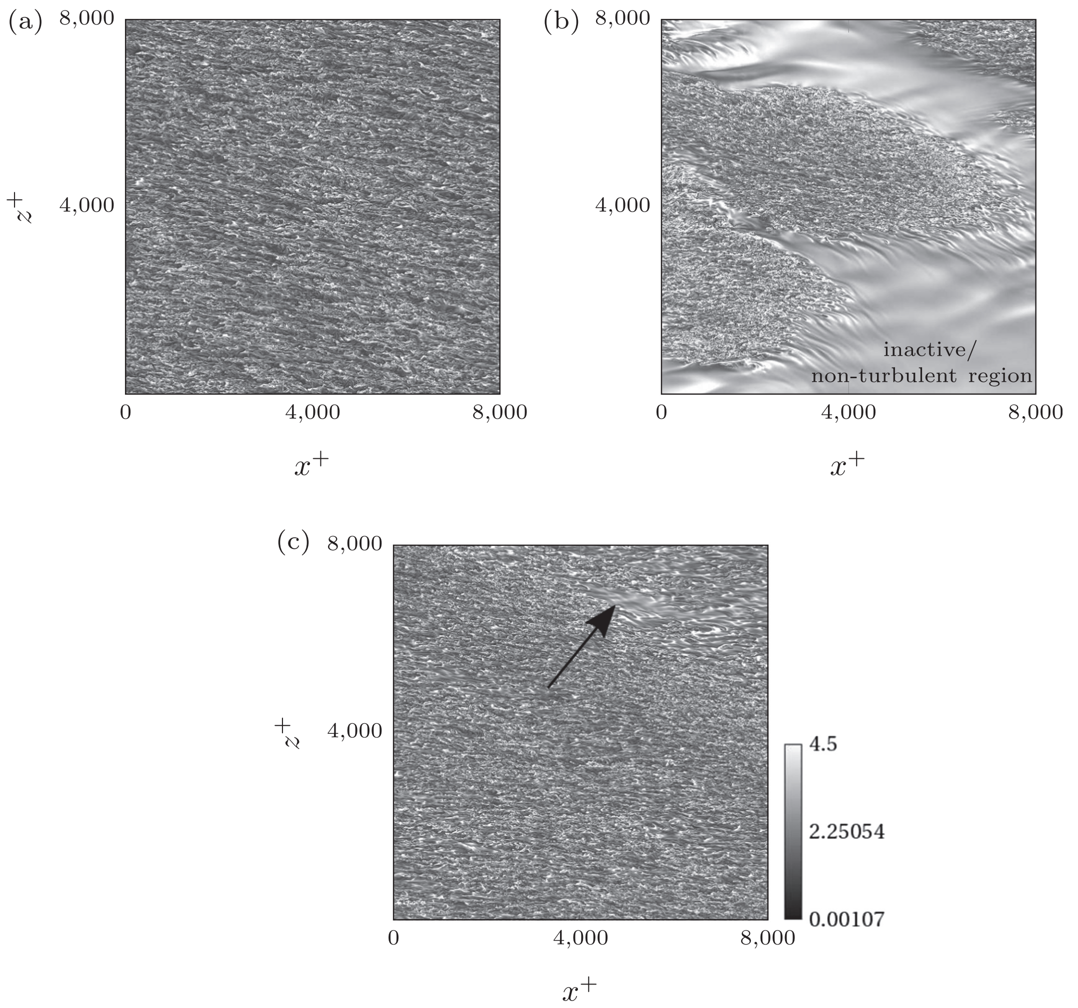

FIG. 6. Vorticity magnitude slices are shown at $y^+ \approx 30$. (a)–(c) correspond to case N, S_1, S_2, respectively. The inactive/non-turbulent regions are visible in both stably stratified cases. Large patches of such relatively quiescent air are clearly visible in (b), whereas an example of a patch is indicated by an arrow in (c).

All other physical parameters are chosen to represent a small perturbation. Therefore, an initial amplitude corresponding to 10 viscous units and a small angle of inclination $\gamma_{\text{initial}} = 0.1°$ are chosen along with a domain length of 200 viscous units. The initial configurations of the hairpins are listed in Table IV.

C. Initial evolution of the hairpin filament

The effect of stable stratification on the evolution of a hairpin filament is studied with the help of the mean background profiles obtained in Sec. IV A. Before discussing the results, we present suitable arguments to address their validity.

TABLE I. The parameters of the DNS simulations used to obtain the background flow $\mathbf{Q_2}$ are listed here. Cases with prefix S indicate stable stratification, whereas N is the neutrally stratified case. The Reynolds number is defined here with the boundary layer height δ_h under neutral conditions, i.e., $\text{Re} = G\delta_h/\nu$, where G is the geostrophic wind velocity magnitude, and ν is the kinematic viscosity. It should be noted that in terms of the laminar Ekman layer depth $D = \sqrt{2\nu/f}$, $Re = GD/\nu = 1000$. However, D loses relevance once the flow becomes turbulent.

Case	Line specification	Bulk Richardson number (Ri_B)	Froude number (Fr)	Reynolds number (Re)
N	————	0	∞	26 450
S_1	…………	2.64	0.02	
S_2	- - - - - - -	0.58	0.07	

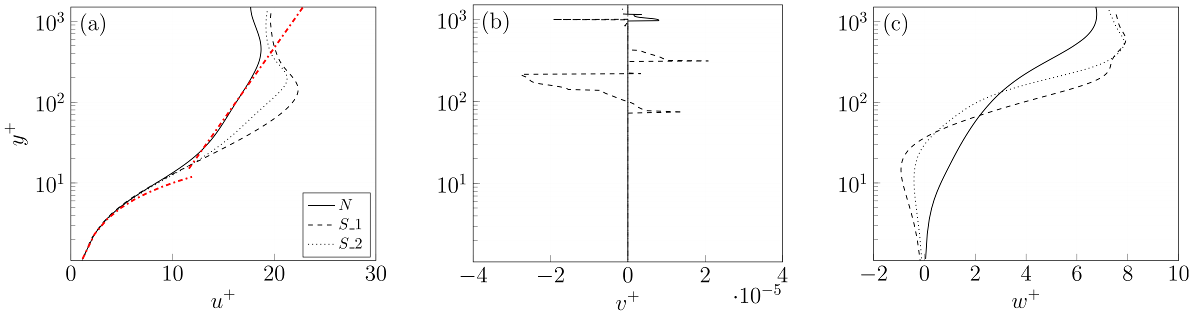

FIG. 7. Mean velocity profiles for every wall-normal height until $y^+ = 1500$ are plotted for all velocity components. $(\cdot)^+$ indicates viscous or wall units. (a)–(c) correspond to the streamwise, wall-normal, and spanwise velocities, respectively. In (a), the red dash dot line shows both the viscous law of the wall $u^+ = y^+$ and the logarithmic law $u^+ = \kappa_v^{-1} \log(y^+) + A$ with the von Kármán constant $\kappa_v = 0.41$ and $A = 5$ for the neutrally stratified case.

TABLE II. The minimum, maximum, and mean values of the dimensionless core size parameter estimated along the centerline of three hairpin-like structures are shown for case N, S_1 and S_2. H1, H2, and H3 are three randomly chosen hairpin-like structures.

Core size parameter	Ekman flow case								
	N			S_1			S_2		
	H1	H2	H3	H1	H2	H3	H1	H2	H3
δ_{min}	0.024	0.016	0.12	0.026	0.17	0.13	0.048	0.025	0.026
δ_{max}	1.26	1.89	1.63	1.92	3.45	5.57	5.79	4.18	1.31
δ_{mean}	0.52	0.49	0.74	0.52	1.1	1.05	0.92	0.70	0.33

(1) As pointed out in the work of Aref and Flinchem,[56] using a Blasius or boundary-layer background profile for $\mathbf{Q_2}$ requires the implementation of a boundary condition at the wall. This is generally achieved with an image vortex placed behind the wall at the same distance as that of the vortex being simulated. However, Aref and Flinchem[56] also argue that including the image vortex is only necessary when the filament is approaching the wall very closely. This was examined by Moin *et al.*[53] who noted that the effect of the image vortex increases as the filament moves closer to the wall. This can be seen in Appendix E, where the image vortex has a stronger impact on the filament evolution at $y^+ = 15$ than at $y^+ = 30$. Hence, image vortices are used only for these two lower heights and ignored for simulations at higher heights.

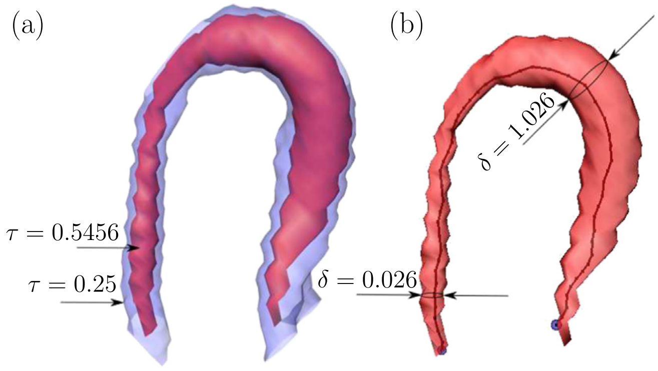

FIG. 8. The uncertainty of core size estimation is shown in (a) where isosurfaces of the same structure at two thresholds of the Q-criterion are visualized. The core sizes are illustrated at two points in (b). Here, τ is the threshold, and δ is the dimensionless core size parameter.

(2) Although the effect of the background flow on the motion of the hairpin filament is studied, it should be noted that this is simply an approximation since there is no feedback mechanism in place, i.e., the action of the filament on the background flow is neglected. Aref and Flinchem[56] show with an order of magnitude estimate that the neglected effect (including vortex stretching) is small provided that the core size of the filament is very small compared to the length scale of the background flow field. This condition is fulfilled in our simulations, in which the core size is several orders of magnitude smaller than the vertical length scale of background flow field.

(3) Viscous effects altering the initial core structure of the filament are also neglected. Moin *et al.*[53] point out that viscous effects become significant only when two vortex cores approach each other closely. This is often cited as a critical drawback of methods based on the Biot–Savart law for vortex reconnection studies, where DNS results show an appreciable deformation of the core even when the core is very small.[57,58] Since reconnecting vortex cores are not the focus of this work, our inviscid core calculations remain valid. Notice, however, that Callegari and Ting[31] provide proper evolution equations for the filament vortex core subject to viscous effects, and the M1 KK method would allow us to straightforwardly include them if needed.

TABLE III. The minimum, maximum, and mean values of the dimensionless core size parameter estimated along the centerline of three hairpin-like structures are shown for case N, S_1, and S_2.

	Ekman flow case								
	N			S_1			S_2		
Circulation	H1	H2	H3	H1	H2	H3	H1	H2	H3
Γ_{min}	0.09	0.018	0.015	0.02	0.049	0.047	0.026	0.0076	0.0014
	−0.107	−0.24	−0.217	−0.042	−0.22	−0.137	−0.01	−0.26	−0.035
Γ_{max}	0.17	0.115	0.318	0.048	0.13	0.11	0.38	0.225	0.049
	−0.009	−0.02	−0.185	−0.048	0.0013	−0.032	−0.0071	−0.0098	0.18
Γ_{mean}	0.134	0.077	0.124	0.034	0.094	0.08	0.202	0.113	0.031
	−0.045	−0.084	−0.204	−0.025	−0.119	−0.071	−0.0425	−0.122	0.11

Their main impact would be a slow thickening of the vortex cores and an associated reduction of the curvature-binormal term in the filament equation of motion.

(4) It should be noted that while the impact of gravity on the motion of the filament is felt through the external background flow obtained from the DNS simulation, its effect on the self-induced motion is not included. From the asymptotic analysis carried out in Sec. VI where the work of Callegari and Ting[31] is extended to include weak gravitational forces, it can be seen that gravity has a contribution only for non-closed and non-periodic filaments that begin and end at different heights. For infinitely long vortex filaments whose ends are at the same height, which are the focus of this work, it is indeed valid to ignore the effect of gravity on their self-induced motion.

For the four initial conditions shown in Table IV, the height of the initial perturbation y^+_{initial} needs to be chosen. From Fig. 1(b), numerous hairpin structures can be seen around $y^+ = 50$. Therefore, at first, $y^+_{\text{initial}} = 50$ is chosen, where various hairpin characteristics are studied with respect to stratification.

Unlike the stagnant background flow cases, the inclination angle for all subsequent simulations is set as $\gamma = 0.1°$, i.e., a near-planar disturbance. The calculation is carried out for all four initial conditions and three background flow profiles with 500 nodes. The results for case S_1 are visualized in Fig. 9 for 140 time steps. This corresponds to a viscous time $t^+ = 7.8$, which is calculated with $t^+ = t\nu/\delta_\nu^2$, where the viscous length scale $\delta_\nu = \nu/u_\tau$. For cases S_2 and N, 140 time steps will correspond to $t^+ = 8.1, 9.75$, respectively. The changes in viscous time units are due to variations in the friction velocity, which is not a fixed parameter in Ekman flow simulations.[9] Henceforth, comparisons among the different stratified cases are made at particular viscous time units instead of time steps.

In accordance with previous simulations of hairpin or parabolic vortex filaments in a shear flow (cf. Hon and Walker[40] and Moin *et al.*[53]), it can be noted from Fig. 9(a) that regardless of the changes in the core size δ and circulation Γ, the head of the filament bends backward and stretches in the wall-normal direction. This curl-up process, as elucidated by Zhou *et al.*,[7] is due to the self-induced velocity of the filament competing with the background mean flow. The formation of the hairpin legs and its movement toward the wall is also observable.

First, changes in the inclination angle $\gamma = \arctan(\Delta y^+/\Delta x^+)$ are calculated for all simulation cases up to $t^+ = 28$ and shown in Fig. 10. Instantly, it can be observed that the initial condition R_2, which has a thicker core and a smaller circulation value, exhibits a relatively slower inclination rate than the other three. On the other hand, the initial condition R_3, which has a thinner core and stronger circulation, shows a faster evolution with a plateauing of the inclination angle around 50°

TABLE IV. The four initial configurations of the hairpin chosen for the simulations with ABL background flow.

Case	Core size (δ)	Circulation (Γ)	Spread (β)	Inclination (γ)	Amplitude (A)	Length (L)
R_1	0.01	0.01	7500	0.1°	10	200
R_2	0.05	0.01				
R_3	0.01	0.05				
R_4	0.05	0.05				

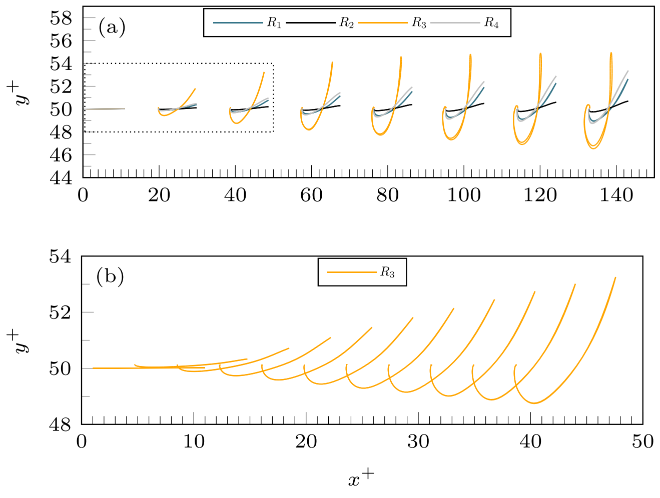

FIG. 9. (a) Temporal evolution for all four initial conditions listed in Table IV is shown here for case S_1. The dotted region is zoomed in for initial condition R_3 in (b).

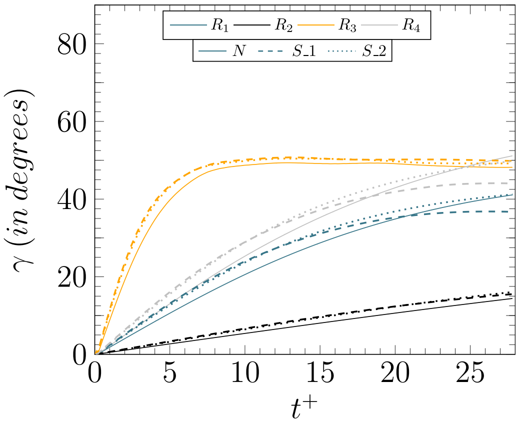

FIG. 10. Time history of the inclination angle γ computed for all four initial conditions from Table IV. The solid, dashed, and dotted lines correspond to the different cases N, S_1, and S_2, respectively.

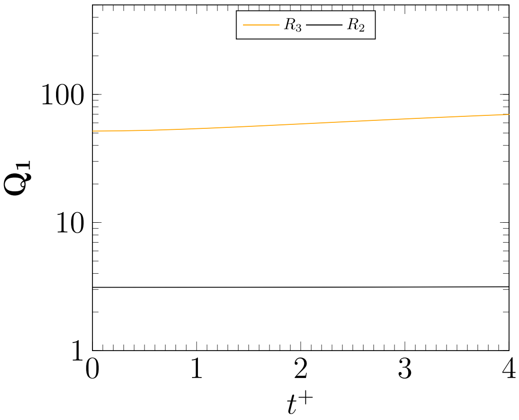

FIG. 11. A comparison of self-induced velocity $\mathbf{Q_1}$ summed over the all nodes of the filament is shown for the initial conditions R_2 and R_3 with the mean background flow of S_1.

for all cases S_1, S_2, and N. This is close to the results reported by Head and Bandyopadhyay[1] who found hairpins inclined at 45° with respect to the wall in the outer regions of the boundary layer.

For initial condition R_3, the differences in the inclination rate and the maximum inclination angle among the neutrally and stably stratified conditions are negligible due to large values of self-induced velocity, which in turn is due to large Γ and small δ. As seen from Fig. 11, the self-induced velocity of R_3, computed by summing up the contributions from all nodes along the filament, is at least 16 times the self-induced velocity of R_2. However, if the self-induced velocity takes smaller values, a clear dependence on the strength of stratification can be educed. An increase in the strength of stratification corresponds to a slower inclination rate. Indeed, if the integration of the initial condition R_2 is carried out for a longer time (not shown), the maximum inclination angle reached is $\gamma_{max} = 18.4°, 22.2°, 28.7°$ for cases S_1, S_2, and N, respectively. This suggests a complex evolution of the hairpin filament strongly hinging on the balance between self-induction and the mean background flow.

D. Further evolution of the hairpin filament

From Sec. IV C, it is clear that R_2 has a slower inclination rate than the other three initial conditions. This means that the development of hairpin features, such as secondary hairpins (as seen in the stagnant flow case and the shear flow case of Hon and Walker[40]), occurs at a much later time. This can be seen in Fig. 12 where secondary hairpins develop at a viscous time $t^+ = 3.9$ with initial condition R_3 and at a much later time $t^+ = 53$ for initial condition R_2. Similar trends (not shown) can be observed with case N and S_2. This hints that the hairpin with initial condition R_2, i.e., with a slower inclination rate, may have a longer lifetime and is therefore further investigated in this subsection. The integration on this initial condition is continued with the three background flow profiles and visualized in the top panel of Fig. 13 where the side view of hairpin filaments is shown. At time $t^+ = 56$, the filaments have been advected downstream in the streamwise direction for 973, 832, and 607 viscous units for case S_1, S_2, and N, respectively. By splitting the flow into turbulent and non-turbulent regions with conditional analysis, Ansorge and Mellado[10]

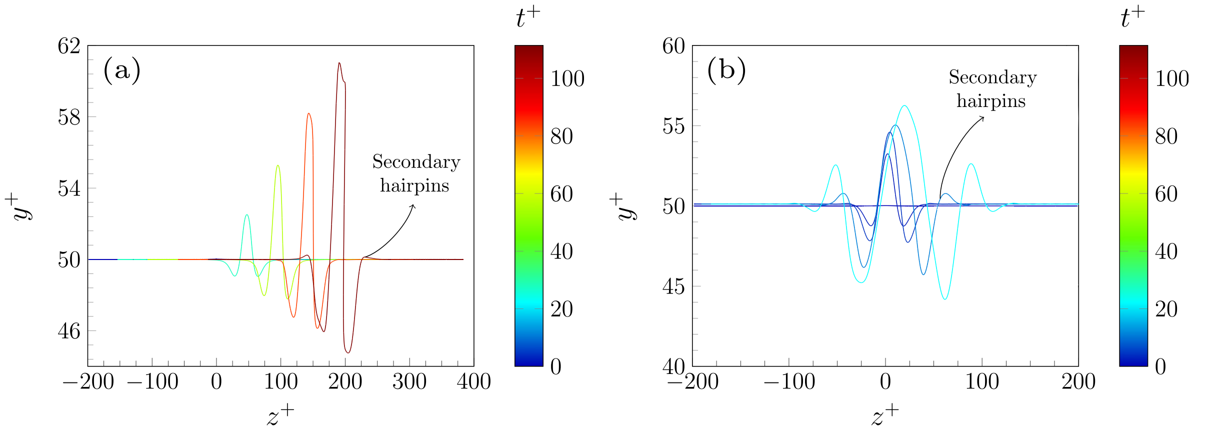

FIG. 12. Temporal evolution of a hairpin filament for case S_1 with (a) initial condition R_2 and (b) initial condition R_3. The filaments are plotted at $t^+ = 0, 27.8, 55.7, 83.5, 111.4$ in (a) and $t^+ = 0, 2.2, 4.4, 11.1, 22.3$ in (b).

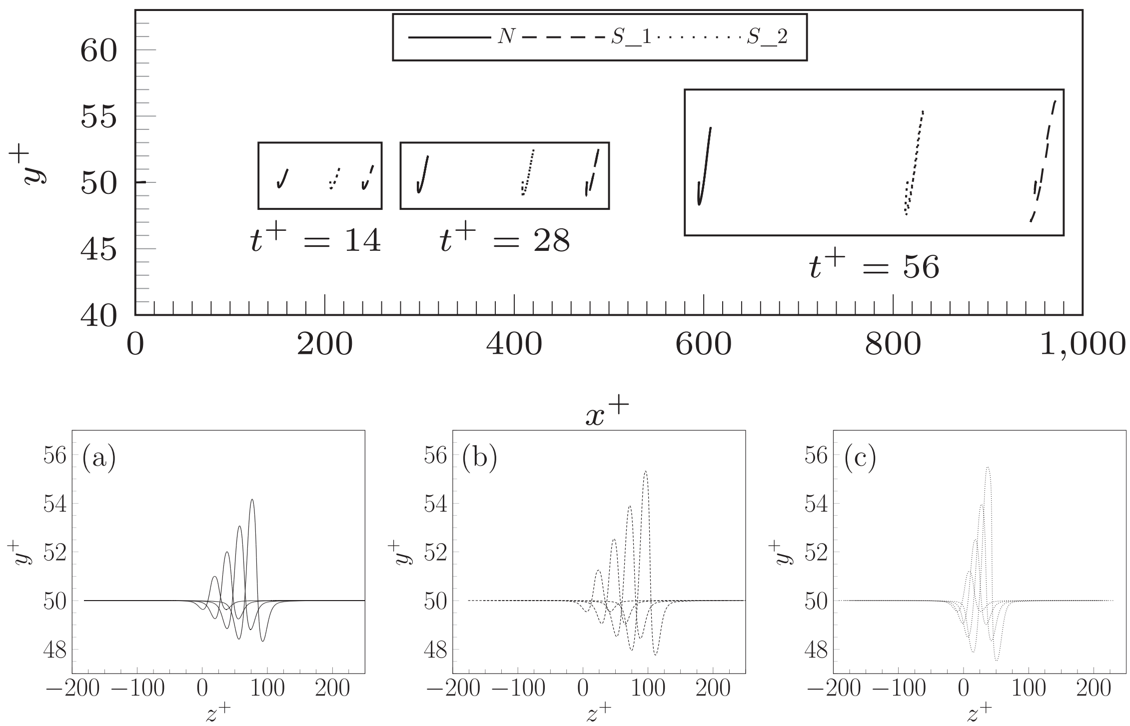

FIG. 13. Temporal evolution for R_2 is shown for cases N, S_1, S_2. The top panel shows a side view of the filaments plotted at $t^+ = 0, 14, 28, 56$ and the bottom panel shows the front view plotted at $t^+ = 0, 14, 28, 42, 56$. In the bottom panel, (a)–(c) correspond to case N, S_1, and S_2, respectively.

show that the streamwise velocity in the turbulent partitions for the strongly stratified case is lower than their non-turbulent counterparts, thereby implying a reduction in the shear intensity in the turbulent regions of the flow. Numerous differences can also be observed from the front view of these hairpins as shown in the bottom panel of Fig. 13.

Although the initial disturbance is symmetric about $z^+ = 0$, an asymmetry develops during the evolution of the hairpin, which is more pronounced for the stably stratified cases. The presence of asymmetric hairpins has been previously reported by Robinson[5] who found after a detailed probing of the DNS of a channel flow that most hairpin vortices tend to be asymmetric. The development of the asymmetry for all background flow profiles can be attributed to the spanwise velocity gradient as seen in Fig. 7(c). As the hairpin stretches in the wall-normal direction, its head encounters a larger spanwise velocity than its leg, which causes the hairpin to tilt in one direction. These results are in line with the presence of an Ekman spiral, within which the wind velocity direction rotates with increasing height[11] The degree of tilt appears to increase with the strength of stratification.

Apart from the asymmetry, the hairpin filament also experiences a strong advection in the spanwise direction. If the midpoint of the hairpin is plotted on a horizontal (*x*, *z*) plane at every instant in time as shown in Fig. 14(a), the neutrally stratified case exhibits a stronger spanwise advection than the stably stratified cases. The spanwise drifts

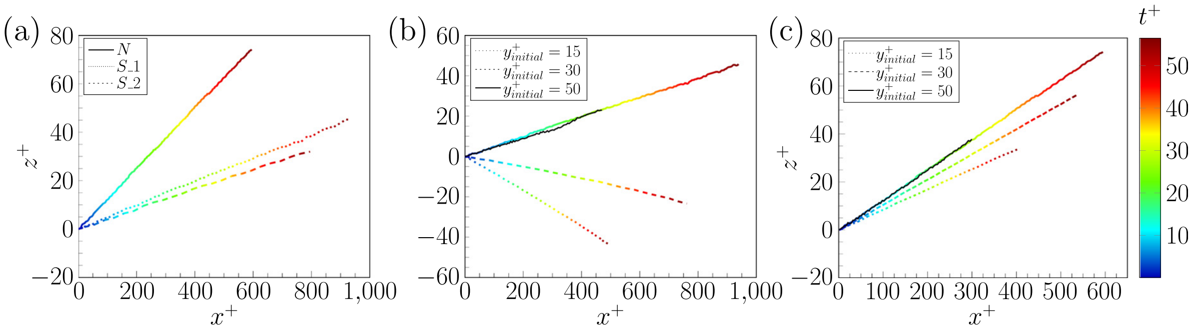

FIG. 14. Comparison of spanwise advection among (a) the three cases N, S_1, S_2 when the hairpin filament is initialized at a height $y^+ = 50$, (b) at three initial heights $y^+_{initial} = 15, 30, 50$ for the strongly stratified case S_1, and (c) at three initial heights $y^+_{initial} = 15, 30, 50$ for the neutrally stratified case N. The solid black line in (b) and (c) shows the spanwise advection with initial condition R_3, whereas all others are shown with initial condition R_2.

(Δz^+), calculated as the spanwise distance traveled by the hairpin from $z^+ = 0$, are 74, 46, and 33 viscous units for cases N, S_1, and S_2, respectively, at time $t^+ = 56$. This character remains unchanged for all initial conditions. For instance, a comparison of R_3 (solid black line) is made with R_2 (solid line with colormap) in Figs. 14(b) and 14(c) for the cases S_1 and N, respectively, where the difference in spanwise advection with both initial conditions is negligible.

If the simulations are repeated for two other initial heights $y^+_{\text{initial}} = 15, 30$ with R_2 as an initial condition, it can be seen from Fig. 14(c) that the neutrally stratified case shows only minor changes in the spanwise advection when compared with $y^+_{\text{initial}} = 50$ and the hairpin filament is oriented anticlockwise with respect to the streamwise direction for all heights. However, the spanwise advection for stably stratified case S_1 shows a change in orientation from the clockwise to anticlockwise direction with an increase in the height [see Fig. 14(b)], which is, again, due to the Ekman spiral. This result suggests that the spanwise orientation of a hairpin filament is linked to its initial height, i.e., its origin. Following Deusebio *et al.*,[59] if the height at which the maximum horizontal velocity is attained is used to estimate the boundary-layer thickness for the strongly stratified case S_1, this is at $y^+ = 156$ viscous units, which is about one-fourth of that observed in the neutrally stratified case. This suggests that all the hairpin simulations were initialized well within the Ekman layer enabling us to observe the spiral as seen in Fig. 14.

V. COMPARISON OF FILAMENT SIMULATION WITH A FEATURE TRACKING SCHEME

The availability of DNS data, which is temporally well-resolved, provides an opportunity to track hairpin-like structures in time. A recent list of the various tracking techniques can be seen in Bußmann *et al.*[60] and references therein. The goal of this section is twofold—first, the volume overlap scheme developed in von Lindheim *et al.*[61] is extended to automatically choose non-subjective, optimum thresholds for the Q-criterion in time. Second, initial conditions are carefully chosen to simulate the motion of a hairpin filament and compare the results with feature tracking. The feature tracking is performed on the strongly stratified case S_1, and the mean velocity profile of the same case is used as a background flow for the simulation.

A. Feature tracking

Following the work of Moisy and Jiménez,[62] we define a coherent structure or feature as a connected set of points within a three-dimensional scalar field, which exceed a threshold, i.e.,

$$\alpha(x) > \tau_p \, \overline{\alpha'^2(y)}^{1/2}, \tag{31}$$

where α is a feature indicator, $\overline{\alpha'^2(y)}^{1/2}$ is its root mean square (RMS) over wall-normal planes, and τ_p is an appropriate threshold. The review paper of Günther and Theisel[63] gives a comprehensive overview of numerous contenders for vortex indicators. In this work, the popular Q-criterion is chosen to identify vortical features.

In a preprocessing step, scalar field Q, normalized with its RMS, is computed for 1000 timesteps and stored locally. For the first time step, a global threshold $\tau_p = 0.0625$ is obtained through percolation analysis.[62,64] Individual structures are extracted with the neighbor scanning algorithm with marching cubes correction[8] (NS+MC). Due to the globally intermittent nature of the flow, which implies the co-existence of large regions non-turbulent motions with turbulent regions, the global threshold value tends to identify a large cluster of structures as an individual structure. Hence, the iterative percolation analysis technique called multilevel percolation (MLP) developed by Harikrishnan *et al.*[8] is used on a small subset of the data to identify and extract individual structures. With manual inspection, one hairpin-like structure is chosen for tracking.

We use the method of volume overlap to track the feature in time. This is a local tracking technique by which the structure extracted at one time step is matched to, or identified with, another at a subsequent time step provided there exists some spatial overlap. The amount of overlap is measured by the dice similarity coefficient (DSC)[65]

$$DSC(I_n, I_{n+1}) = \frac{2|I_n \cap I_{n+1}|}{|I_n| + |I_{n+1}|}, \tag{32}$$

where I_n and I_{n+1} are the structures at time t_n and t_{n+1}, respectively, and $|\cdot|$ is the volume of the structure. The value of DSC can range between 0 and 1, where 1 indicates a perfect overlap. The tracking proceeds only when DSC is greater than the user-defined overlap threshold $\tau_{overlap}$. In our case, $\tau_{overlap} = 0.5$.

Another important parameter that needs to be set is the threshold τ for subsequent timesteps. In the first run, a constant threshold of $\tau = 1.399$ is used. The results are shown in Fig. 15(a), in which both volume rendering and the centerline of the structure are shown. The centerline is again obtained by the block-wise skeletonization method of Fouard *et al.*[54] The tracking suggests that the hairpin structure is constantly shrinking in time. This is expected since constant thresholding in time does not adapt to the dynamical changes in the size of a structure. This limitation is overcome by combining volume overlap with multilevel percolation analysis. In essence, this technique accommodates for the growth or deterioration of a structure by dynamically adjusting the thresholds in time. The details of this technique, henceforth referred to as multilevel percolation thresholding in time (MLPT), are presented in Appendix D. The result as shown in Fig. 15(b) suggests that the hairpin structure grows in the size until $t^+ = 42.5$, after which it starts shrinking. Further details of the hairpin-like structure, such as the temporal evolution of inclination angle, streamwise, spanwise, and wall-normal extents, are compared between both methods in the supplementary material.

B. Comparison with filament simulation

The hairpin-like structure tracked with MLPT thresholding is visualized in Fig. 16. Since it is clear that this structure exists in the outer layer in the range of $80 < y^+ < 180$, the filament simulation is also initialized at a higher wall-normal height $y^+_{\text{initial}} = 125$ to enable an appropriate comparison. A larger amplitude $A = 80$ and, correspondingly, a larger initial width are also chosen. All initial conditions are listed in Table V. With a spatial discretization of 1500 nodes, the simulation is carried out until the overlap condition (C2) is violated.

Since the initial state of the hairpin structure from the DNS dataset is unknown and the structure is tracked from a later point in its lifetime, it is not possible to establish a direct comparison of the tracking results with the filament simulation. However, some qualitative comparisons can be drawn. The streamwise advection of the hairpin structure, tracked in time for 674 time steps or 84 viscous time units, is

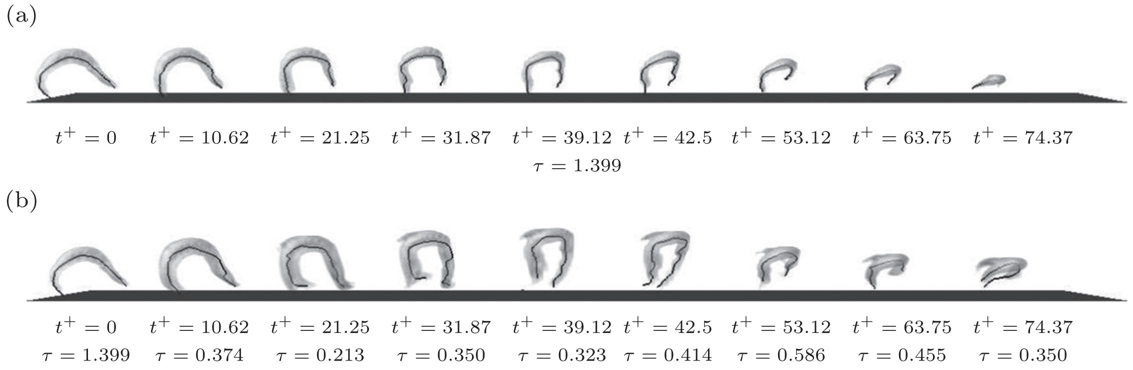

FIG. 15. Track of a hairpin-like structure with (a) constant thresholding and (b) MLPT thresholding. The complex geometry of the extracted structures may result in a network of centerlines. Since we are only interested in the main centerline defining the hairpin structure, the remaining are discarded.

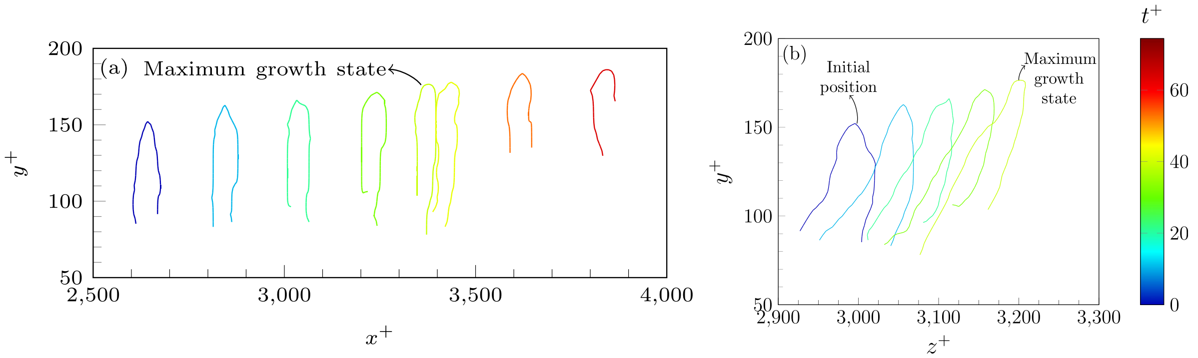

FIG. 16. Temporal evolution of the tracked hairpin-like structure with MLPT thresholding as seen in Fig. 15(b). (a) and (b) The side view and the front view of the feature tracking results, respectively.

1621 viscous units. The filament simulation shows a streamwise advection of 1682 viscous units over the same viscous time. This minor discrepancy can be attributed to the choice of the initial height for the filament simulation suggesting that the hairpin structure in the DNS simulation may have originated from a lower height. Differences may also arise due to mutual induction effects of neighboring hairpin structures. It can be seen from Fig. 17 that even at the initial state of the tracked hairpin structure (highlighted blue), at least one other hairpin

TABLE V. Initial condition for comparison with feature tracking results.

Parameter	Value
Core size parameter, δ	0.01
Circulation, Γ	0.05
Spread parameter, β	500
Amplitude, A	80
Angle of inclination, γ	0.1°
Initial wall-normal position, y^+_{initial}	125
Domain length, L	400

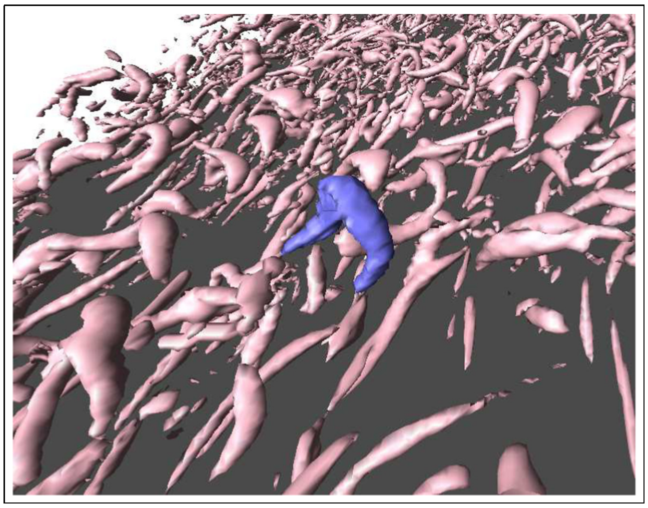

FIG. 17. Isosurfaces of the *Q*-criterion for case S_1 are shown here for the initial time step. The structure tracked with MLPT is highlighted in blue.

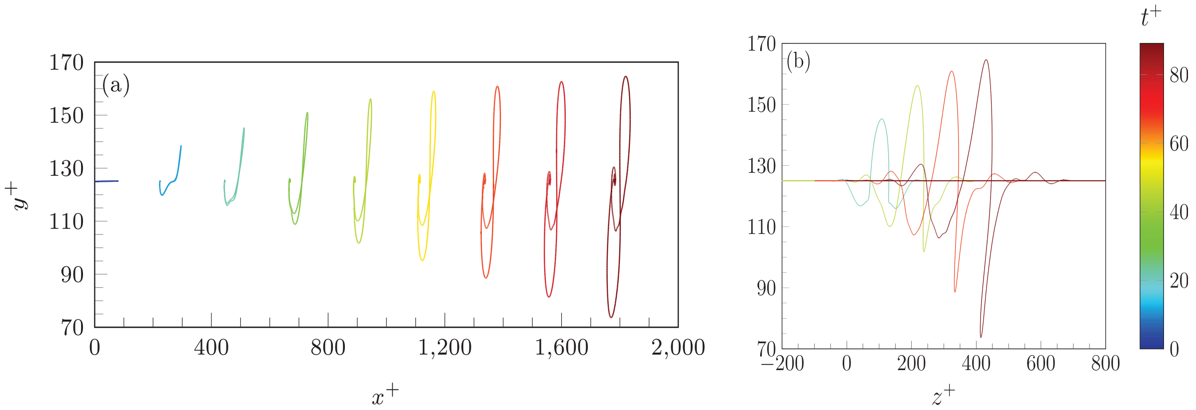

FIG. 18. Temporal evolution for a larger hairpin filament at $y^+_{\text{initial}} = 125$. (a) and (b) The side and front view of the temporal development, respectively.

structure can be seen in close proximity. This may have a strong influence on the later developments of the tracked hairpin structure.

The initial state of the DNS hairpin structure as seen from Fig. 16 shows that the hairpin, although asymmetric, has both legs at similar wall-normal heights of 91 and 85 viscous units. Over time, at its maximum growth state, the asymmetry grows further with one leg at a wall-normal height of 78 viscous units and the other at 103 viscous units. A similar effect can be observed in Fig. 18(b). At time $t^+ = 84$, both legs of the hairpin are at a wall-normal height of 73 and 106 viscous units. As described in the further evolution part of Sec. III, the persistence of asymmetry over time is due to the influence of spanwise velocity. Unlike the results reported in Zhou *et al.*,[7] who suggested that a sufficiently strong asymmetrical initial configuration is necessary to produce an asymmetrical hairpin vortex, our results indicate that asymmetry develops naturally as a consequence of the mean background flow.

VI. INFLUENCE OF BUOYANCY—AN ASYMPTOTIC ANALYSIS

In all the hairpin filament simulations presented in this paper, the effect of gravity on the self-induced motion of the filament is ignored. While we expect the effects of gravity to be predominantly felt through its impact on the external flow, gravity may also have a minor impact on the self-induced velocity of the filament. In this section, we present the results of an asymptotic analysis, which provides the conditions under which gravitational forces can be ignored, consequently justifying the neglect of gravity in the presented simulation results. The analysis is an extension of the work by Callegari and Ting[31] including weak gravitational forces; as the influence of gravity is assumed to be weak, the leading and first order equations for the internal flow field will agree with Callegari and Ting.[31] As a consequence, the expression for the core constant, which couples the self-induced velocity of the filament to the flow inside the vortex core, will be the same as in Callegari and Ting,[31] with the effect of gravity only entering in the compatibility conditions, which determine the temporal evolution of the axial and radial velocity components of the internal flow. The complete derivation can be found in Appendix F; here, we will merely give a brief overview of the method and the relevant results.

The idea upon which the analysis is based is as follows—the self-induced motion of the filament is dictated by an inner solution, describing the flow inside the tube-like structure, and the outer flow, which is simply given by the line Biot–Savart law, is reiterated

$$\mathbf{Q}_1(\mathbf{P},t) = -\frac{\Gamma}{4\pi}\int_{\mathscr{L}} \frac{\left(\mathbf{P}-\mathbf{X}(s',t)\right)\times \mathbf{ds}'}{\left|\mathbf{P}-\mathbf{X}(s',t)\right|^3}, \tag{33}$$

where $\mathscr{L}$ is the vortex centerline, $\mathbf{X}(s,t)$ is the position vector for any point on $\mathscr{L}$, which is parametrized by the arc length parameter s, and $\mathbf{P}$ denotes a point outside of the filament core [see Fig. (27)]. A careful expansion of the integrand in the Biot–Savart formula leads to an expression for the behavior of $\mathbf{Q}_1$ as the radial distance to the filament goes to zero

$$\mathbf{Q}_1(P,t) = \frac{\Gamma}{2\pi r}\hat{\theta} + \frac{\Gamma}{4\pi R}\left[\ln\left(\frac{R}{r}\right)\right]\hat{b} + \frac{\Gamma}{4\pi R}(\cos\phi)\hat{\theta} + \mathbf{Q}_f, \tag{34}$$

where $\hat{\theta}$ is the unit circumferential vector, and $\hat{b}$ is the unit binormal vector, associated with the point s on the vortex filament $\mathbf{X}(s,t)$. $R = R(s,t)$ is the local radius of curvature, and Γ is the circulation of the filament. The vector $\mathbf{Q}_f$ is a part of the Biot–Savart integral, which has a limit as $r \longrightarrow 0$. Since the Biot–Savart integral diverges on the filament centerline, it cannot be used to determine the motion of the velocity of the vortex core itself. To overcome this problem, we follow Callegari and Ting[31] and employ a matched asymptotic expansion, where the outer solution, given by Eq. (34), is matched with an inner solution derived from the Navier–Stokes equations with suitable boundary conditions. The analysis rests on the assumption that gravitational forces are weak and only enter in the second order equations in the asymptotic expansion.

The equations for the binormal and normal components of the filament velocity remain unchanged as compared with Callegari and Ting[31] and can be written as

$$\hat{b}\cdot\dot{\mathbf{X}}^{(0)} = \hat{b}\cdot\mathbf{Q}_0 + \kappa^{(0)}\frac{\Gamma}{4\pi}\left(\ln\frac{R^{(0)}}{\varepsilon} + C(t)\right), \tag{35a}$$

$$\hat{n}\cdot\dot{\mathbf{X}}^{(0)} = \hat{n}\cdot\mathbf{Q}_0, \tag{35b}$$

where $\varepsilon = (\nu/\Gamma)^{1/2}$ and $R^{(0)} = 1/\kappa^{(0)}$ is the leading order radius of curvature, and $\mathbf{Q}_0$ is the superposition of the finite part of the

Biot–Savart integral and the background flow. $C(t)$ denotes the core constant and is given by

$$C(t) = 2\left[\frac{1}{2}\lim_{\bar{r}\to\infty}\left(\frac{4\pi^2}{\Gamma^2}\int_0^{\bar{r}}\xi\left(v^{(0)}\right)^2 d\xi - \ln\bar{r}\right) - \frac{1}{4} - \frac{4\pi^2}{\Gamma^2}\int_0^{\bar{r}}\xi\left(w^{(0)}\right)^2 d\xi\right], \tag{36}$$

where $v^{(0)}$ and $w^{(0)}$ denote the leading order circumferential and axial velocity components of the internal flow field. Note that the leading order velocity components are only functions of the compressed radial coordinate $\bar{r}$. For the complete derivation, we refer the reader to Appendix F.

We should note here that, by the vorticity-based analysis given by Klein and Knio,[32] the core constant can also be written as

$$C(t) = -\frac{1}{2} - \frac{2\pi}{\Gamma}\int_0^{\infty}\left[\frac{1}{\kappa}\zeta_{11}^{(1)} + \bar{r}\ln\bar{r}\,\zeta^{(0)}\right]d\bar{r}, \tag{37}$$

where $\zeta^{(0)}$ is the leading order vorticity given by

$$\zeta^{(0)} = \frac{1}{\bar{r}}\left(\bar{r}v^{(0)}\right)_{\bar{r}}, \tag{38}$$

and $\zeta_{11}^{(1)}$ is the first cosine Fourier mode of the first order vorticity $\zeta^{(1)}$ with respect to θ,

$$\zeta_{11}^{(1)} = \frac{1}{2\pi}\int_0^{2\pi}\zeta^{(1)}(\bar{r},\theta,s,t)\cos\theta\, d\theta. \tag{39}$$

Since the core constant depends on the leading order circumferential and axial velocity components, additional equations for the temporal evolution of $v^{(0)}$ and $w^{(0)}$ are required to completely determine the self-induced filament velocity. These equations are derived from the symmetric second-order radial and axial velocity equations, as well as the symmetric second-order continuity equation, and it is first here that the effect of gravity enters. The derivation rests on the assumption that the leading order velocity, pressure, and temperature components are all axially symmetric; an assumption that is justified by the symmetry of the outer flow field. We additionally make the simplifying assumption that density variations are only due to temperature variations and not pressure variations. Consequently, the energy equation simplifies to that of a Boussinesq fluid, and the density perturbations can be assumed to decay exponentially as $\bar{r} \to \infty$.

For either closed vortex filaments or filaments, which are symmetric in some horizontal direction, we get the following evolution equations for the axial and radial velocity components:

$$\left(w_t^{(0)} - \frac{\bar{\nu}}{\bar{r}}\left(\bar{r}w_{\bar{r}}^{(0)}\right)_{\bar{r}}\right)S^{(0)}(t) = \frac{1}{2}\bar{r}^3\left(\frac{w^{(0)}}{\bar{r}^2}\right)_{\bar{r}}\dot{S}^{(0)}(t) + \alpha g\int_0^{S_0}\hat{\mathbf{y}}\cdot\hat{\boldsymbol{\tau}}\sigma^{(0)}\tilde{T}^{(0)}ds, \tag{40}$$

$$\left(v_t^{(0)} - \bar{\nu}\left[\frac{1}{\bar{r}}\left(\bar{r}v_{\bar{r}}^{(0)}\right)_{\bar{r}} - \frac{v^{(0)}}{\bar{r}^2}\right]\right)S^{(0)}(t) = \frac{1}{2}\frac{\left(\bar{r}v^{(0)}\right)_{\bar{r}}}{\bar{r}}\dot{S}^{(0)}(t). \tag{41}$$

Here, $S^{(0)}$ is the leading term in the expansion for the arc length at time t and is related to the stretching parameter $\sigma^{(0)}$ by $\sigma^{(0)} = \tilde{S}_s^{(0)}$. Except for the second term appearing on the right-hand side of 40, the evolution equations are identical to the compatibility conditions found by Callegari and Ting.[31] In principle, due to the second term on the right-hand side of 40, one would need a third evolution equation, namely, one for the leading order temperature perturbation $\tilde{T}^{(0)}$ to close the system. However, as we shall see the, as a consequence of the assumption of axial symmetry, the gravity term disappears leaving us with the evolution equations of Callegari and Ting.[31] To see this, note that since we have assumed that all the leading order field components are independent of s, we can write

$$\int_0^{S_0}\hat{\mathbf{y}}\cdot\hat{\boldsymbol{\tau}}\sigma^{(0)}\tilde{T}^{(0)}ds = \tilde{T}^{(0)}(\bar{r},t)\int_0^{S_0}\hat{\mathbf{y}}\cdot\hat{\boldsymbol{\tau}}\sigma^{(0)}ds. \tag{42}$$

The integrand can be written as

$$\hat{\mathbf{y}}\cdot(d\mathbf{X}), \tag{43}$$

thus implying that

$$\int_0^{S_0}\hat{\mathbf{y}}\cdot\hat{\boldsymbol{\tau}}\sigma^{(0)}ds = \int_0^{S_0}\hat{\mathbf{y}}\cdot(d\mathbf{X}) = \hat{\mathbf{y}}\cdot(\mathbf{X}(S_0) - \mathbf{X}(0)). \tag{44}$$

This is nothing but the height difference between the initial and final points of the filament. Thus, we can conclude that in the case of closed filament, the gravity term vanishes. Furthermore, if the ends of an infinite vortex filament are at the same height, this term will also vanish, indicating that the only time we get a contribution from gravity in the regime outlined here, is when we have an infinitely long filament, which is tilted with respect to the vertical direction, thus breaking the horizontal symmetry. This rather curious result is partially due to having assumed that the leading order velocity components are axially symmetric, meaning that one cannot have regions of acceleration (deceleration) of the flow along the centerline. Thus, in the case of closed or horizontally periodic vortex filaments, the influence of gravity on the internal flow vanishes and we can conclude that it was indeed valid to ignore gravity in the numerical simulations in Secs. II–V.

VII. SUMMARY AND CONCLUSIONS

In this work, we investigated the abundance and orientation of hairpin vortex structures in the strongly stratified Ekman flow reported in Harikrishnan *et al.*[8] To study the motion of these structures, we treat them as slender vortex filaments, where the diameter of the vortex core d is much smaller than its characteristic radius of curvature R.

First, the evolution of the hairpin filament is studied in a stagnant background flow with two methods: the local induction approximation (LIA) and the corrected thin-tube model of Klein and Knio[32] with the M1 optimization technique[39] (M1 KK). The results of both methods indicate that the tip region (or head) of the hairpin vortex moves backward and downward rapidly and are able to correctly capture the corkscrew shape (in the side view) as shown in Hon and Walker.[40] However, if the initial width of the hairpin filament is reduced, i.e., for $\beta = 50$ as shown in Figs. 5(b) and 5(d), a marked difference can be observed in the development of the legs between LIA and the M1 KK scheme, the latter of which can represent the nonlocal effects accurately.

With the M1 KK scheme, the motion of hairpin filaments with an ABL background flow was studied for three cases: two stably stratified (S_1, S_2) cases at different degrees of stratification and a neutrally stratified (N) case. The hairpin filament was initialized as a small, nearly two-dimensional perturbation, and simulations were run for four different initial conditions with varying core size (δ) and circulation (Γ). For all four initial conditions, the near-planar perturbation becomes three-dimensional as a result of the self-induced velocity of the filament, which induces the head of the hairpin vortex to bend backward away from the wall, thereby increasing the inclination angle (γ). In particular, we note the following:

1. For the initial condition R_3, which has a relatively thinner core and stronger circulation resulting in a large self-induced velocity, the differences in inclination rate and maximum inclination are negligible for all background flow profiles.
2. For all other initial conditions, it can be seen that an increase in stratification results in a slower inclination rate and a smaller maximum inclination angle.
3. Since the effect of rotation is present in the Ekman flow, it can be seen that the hairpin filament, which is initially symmetric about $z^+ = 0$, becomes asymmetric over time, thereby tilting the vortex. As expected, the degree of tilt increases with an increase in the strength of stratification. Tracking of the Q-criterion structure in the DNS dataset shows that the asymmetry becomes stronger as the structure grows in size.
4. Apart from advecting in the streamwise direction, the hairpin filament also experiences strong advection in the spanwise direction. Initializing the filaments at three different heights $y^+ = 15, 30, 50$, we observe an appreciable change in their spanwise orientation, particularly for the strongly stratified case S_1. The spanwise orientation changes from clockwise to anticlockwise (with respect to the streamwise direction) with an increase in the height. This hints that, under stable stratification, hairpin filaments initialized at the same height may have a similar spanwise orientation.

Although we present a link between the spanwise orientation of the hairpin filament and its initial starting height for the very stable regime, it is still not clear if this is solely responsible for the similar orientation of these structures in different regions of the flow witnessed in Harikrishnan *et al.*[14,15] Further probing of the DNS dataset is necessary with hairpin-like structures and their interactions, which need to be tracked in time. Our current efforts are focused in this direction. Further efforts can be directed toward studying the impact of mutual induction of neighboring hairpin filaments (where viscous effects become important) on their orientation. An extension of the M1 KK method incorporating the viscous diffusion has already been presented in Klein *et al.*[66] This should lead to a straightforward modification of our slender vortex filament code. Additionally, the asymptotic analysis from Sec. VI can be continued to obtain a new core constant $C(t)$, which can be directly implemented in our slender vortex code to quantify the effect of gravity on the self-induced motion of the filament. We emphasize the need to study the dynamics of hairpin filaments/structures, particularly in the very stable regime, as it is still a poorly understood element of the atmospheric boundary layer.[67]

SUPPLEMENTARY MATERIAL

See the supplementary material where further details of the tracked hairpin-like structure (from Sec. V), such as the temporal evolution of inclination angle, streamwise, wall-normal, and spanwise extents, are compared when tracked with constant and MLPT thresholds.

ACKNOWLEDGMENTS

The authors would like to thank Professor Omar M. Knio for lending support and helpful discussions during the initial stages of the work. They would also like to thank Dr. Cedrick Ansorge, who performed the DNS simulations of the stratified Ekman flows and provided access to the Jülich Supercomputing Center, where the data are stored under the project dns2share. This research is funded by the Deutsche Forschungsgemeinschaft (DFG) through Grant No. CRC 1114 "Scaling Cascades in Complex Systems," Project No. 235221301, and Project B07: Self-similar structures in turbulent flows and the construction of LES closures. Marie Rodal gratefully acknowledges the support of the Research Fund of the University of Antwerp.

AUTHOR DECLARATIONS

Conflict of Interest

The authors have no conflicts to disclose.

Author Contributions

Abhishek Paraswarar Harikrishnan: Conceptualization (equal); Data curation (lead); Formal analysis (equal); Investigation (equal); Software (lead); Visualization (lead); Writing – original draft (lead); Writing – review & editing (equal). **Marie Rodal:** Formal analysis (lead); Investigation (equal); Software (equal); Visualization (supporting); Writing – original draft (lead); Writing – review & editing (equal). **Rupert Klein:** Supervision (equal); Writing – original draft (equal); Writing – review & editing (equal). **Daniel Margerit:** Software (supporting); Writing – review & editing (equal). **Nikki Vercauteren:** Conceptualization (lead); Supervision (equal); Writing – original draft (equal); Writing – review & editing (equal).

DATA AVAILABILITY

The code developed for the motion of slender vortex filaments during the course of this work is written in python. This is based on the EZ-vortex code,[43] which was written in C. The python code and the mean velocity profiles from the DNS database are available at the GitHub repository: https://github.com/Phoenixfire1081/SlenderVortexSimulation.

APPENDIX A: VALIDATION OF THE CODES

Here, the static test presented in Sec. 5.2 of Klein and Knio[32] is used to validate our slender vortex code. This test, which compares the velocity predictions of both LIA and M1 KK schemes, eliminates the possibility of errors introduced during temporal discretization due to its static nature. The equation for generating a sinusoidal plane curve is reiterated as

$$\mathbf{X}(s) = s\mathbf{t} + \varepsilon^2 \tilde{a}\ \sin(2s/\varepsilon)\mathbf{n}, \tag{A1}$$

where $\mathbf{t}$ and $\mathbf{n}$ are mutually orthogonal unit vectors, $\tilde{a}$ is the amplitude, and s is a linear spacing of node locations satisfying the overlap condition. The test is performed with the following parameters: $\delta = 0.01$, $\varepsilon^2 = 0.25$, $\Gamma = 4\pi$, $\tilde{a} = 0.01$. It is easy to check that a minimum of $N = 316$ nodes are necessary to satisfy the overlap

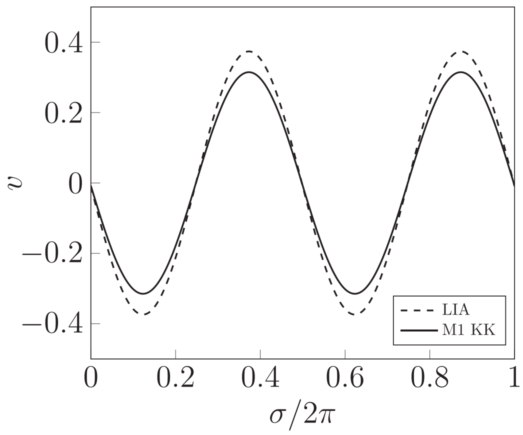

FIG. 19. Binormal velocity prediction for the plane curve shown in A1 with LIA (dashed line) and the M1 KK (solid line) methods.

condition from Eq. (9). However, 1024 nodes are chosen to eliminate numerical inaccuracies in this test. The choice of mutually orthogonal vectors will induce a velocity normal to the plane, i.e., in the direction of $\mathbf{b} = \mathbf{t} \times \mathbf{n}$. Therefore, the velocity prediction along $\mathbf{b}$ is shown in Fig. 19. The maximum deviations in velocity predictions between LIA and M1 KK methods is about 19%. While this is slightly lower than the 25%–30% reported in Klein and Knio[32] who compared the asymptotic predictions of the Klein–Majda scheme with LIA, the differences clearly highlight the overestimation of velocity by LIA, which excludes non-local effects of vortex self-induction.

APPENDIX B: IMPACT OF RESOLUTION ON VELOCITY PREDICTION

For the test shown in Appendix A, the number of nodes N is varied and all other parameters are held constant. N is increased in increments of 50 starting from 100 nodes and is tested until 1500. The results in Fig. 20 show that after overlap is satisfied (shaded red region), the deviation between the maximum velocity with 316 nodes, which is the minimum number of nodes necessary for overlap, and 1500 nodes is less than 0.5%. Therefore, one can surmise that the minimum number of nodes, henceforth referred to as *minimum overlap*, gives satisfactory velocity predictions.

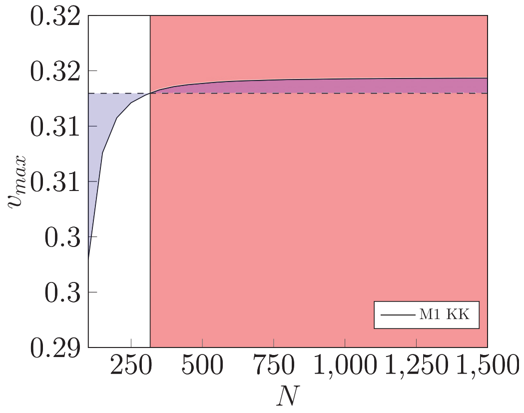

FIG. 20. Maximum binormal velocity for the plane curve shown in A1 with M1 KK (solid line) for various values of N. The dashed line shows the maximum velocity with $N = 316$, which satisfies the overlap condition in Eq. (9) and the blue shaded region shows the deviation. The red shaded region shows all N satisfying the overlap condition.

APPENDIX C: CHOICE OF PARAMETERS

With minimum overlap satisfied, the optimum values for three parameters are identified in this section. First, the number of images P is varied from 1 to 100, and the maximum binormal velocity is computed in each case. From Fig. 21, it can be seen that the velocity prediction shows no deviations for $P \geq 7$. In all subsequent simulations, we choose $P = 8$.

The parameter K defined in Eq. (24) is a ratio between the maximum element length along the filament, and the core size can be thought of as an overlap parameter. To estimate this parameter, we use method 2 velocity correction approach of Knio and Klein.[39] The corrected velocity is given by

$$\boldsymbol{v}_{\text{corr}}^{\text{ttm}} = \boldsymbol{v}_{\boldsymbol{I}} + \frac{\Gamma}{4\pi} \ln\left(\frac{\sigma_1}{\delta^{\text{ttm}}}\right) \kappa \mathbf{b}, \tag{C1}$$

where σ_1 is described in Eq. (24). It can be noted from Fig. 22 that the maximum binormal velocity predictions show less deviations for larger values of K when the nodes are increased. A similar trend can be observed for the parameter ϕ in Fig. 23. Therefore, to keep the numerical errors low, the overlap condition is modified as

$$\underset{i=1..N}{max} |\delta \boldsymbol{\chi}_i| < \frac{\delta}{3}. \tag{C2}$$

Although this increases the number of nodes necessary for computation threefold, it ensures that the velocity predictions will have sufficient accuracy for each time step. For all simulations in this work, $K = 3$ and $\phi = 2$.

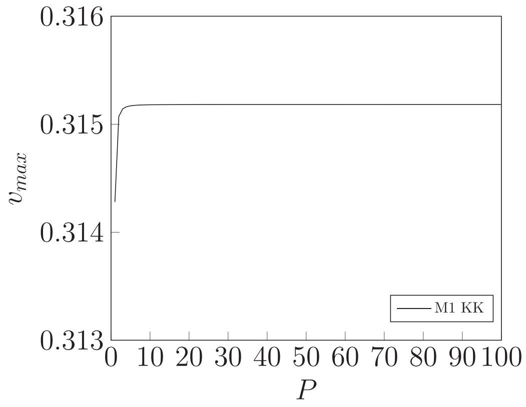

FIG. 21. Maximum binormal velocity for the plane curve shown in A1 with M1 KK (solid line) for various values of P.

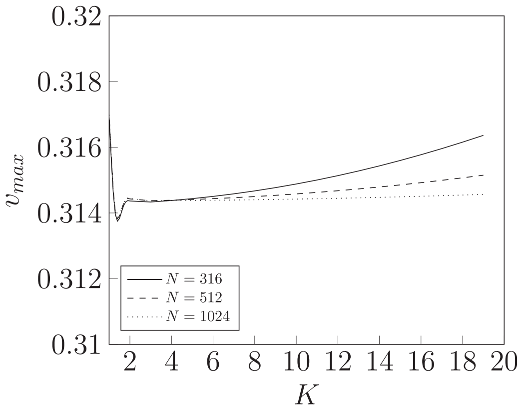

FIG. 22. Maximum binormal velocity for the plane curve shown in A1 with M1 KK for various values of K. The solid, dashed, and dotted lines show the differences with the number of nodes N.

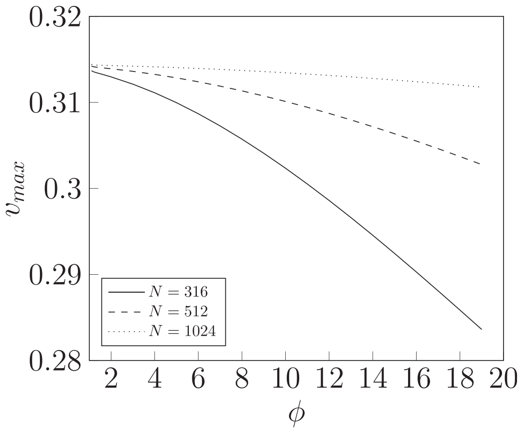

FIG. 23. Maximum binormal velocity for the plane curve shown in A1 with M1 KK for various values of ϕ. The solid and dashed show the differences with the number of nodes N.

APPENDIX D: MULTILEVEL PERCOLATION THRESHOLDING IN TIME

To overcome the limitation of using a constant threshold in time, we introduce a novel thresholding scheme based on multilevel percolation analysis (MLP).

The MLP scheme, where percolation analysis is applied in an iterative manner, relies on the definition of simple and complex structures to identify an optimum threshold. Given a scalar field, the ratio $V_{\max}/V$ (where $V_{\max}$ is the volume of the biggest structure in the domain and V is the volume of all structures) is computed over the entire range of threshold values. When $V_{\max}/V = 1$ for the entire threshold range, there exists exactly one structure. This type of structure is denoted *simple* because when the threshold is increased, the structure collapses to a single local maximum. A *complex* structure is encountered when $V_{\max}/V$ falls below 1 over the entire threshold range, i.e., two structures may co-exist. In practice, using $V_{\max}/V = 1$ to find simple structures is computationally intensive and is therefore relaxed to $V_{\max}/V > 0.5$, which implies that at most two structures can co-exist where one structure always has a volume larger than the other. These definitions are used to identify optimum thresholds in time. This method, henceforth called as the overlap method with multilevel percolation thresholding in time (MLPT), is discussed as follows:

(1) Once the structure to be tracked is chosen by the user, the NS+MC extraction algorithm is used to extract the structure at the MLP threshold from the scalar field.
(2) First, the algorithm checks for structure growth [see Fig. 24(a)] by decreasing the threshold in the subsequent time step. In our case, the minimum threshold to check is taken to be the global percolation threshold, τ_p. However, in practice, the minimum value to check is restricted only by the indicator itself. For instance, with Q-criterion, smaller thresholds can be checked as long as $Q > 0$.
(3) For every threshold being tested, a structure at timestep $n + 1$ is found by overlapping the structure at timestep n. Once the t_{n+1} structure is found, it is extracted and subjected to MLP to determine if it is a simple or complex structure. If the structure is found to be simple, the threshold is increased and the process is repeated until a complex structure is found. This signals the algorithm that a previous threshold is the optimum one.
(4) If the overlapped structure at t_{n+1} is complex at the MLP threshold itself, then the algorithm checks if the structure is shrinking in time [see Fig. 24(b)] by increasing the threshold.
(5) Steps 2–4 are repeated for every timestep.

Optimization: Since hairpins are small-scale features that need to be tracked in a large domain of size $1024 \times 256 \times 2048$ (approximately 2 GB for single precision, raw binary format) per time step, the procedure described above can become computationally expensive. Therefore, two key optimization steps are used:

(1) Since we use temporally well-resolved DNS data for tracking, it can be assumed that the structure is not advected too far in the domain for every time step. Once the initial structure is extracted at the first time step, a smaller domain around the structure of interest can be searched in the subsequent time step, which restricts the search space for the extraction algorithm. The smaller computational domain is then moved in time.
(2) To reduce RAM overhead, specific bytes of data corresponding to the smaller computational domain are read into memory.

With both optimizations, the structure in Fig. 15(b) was tracked for 674 time steps (or 1.4 TB of data) in under 7 h.

APPENDIX E: IMPACT OF IMAGE VORTICES

The boundary condition of a rigid wall is enforced with the help of an image vortex. In this scenario, an additional step is included in the calculation after step 3 of the summary presented in Sec. II. The image vortex also has two contributions as shown in 20, i.e., from the central part of the domain and its images on the left and right side to enforce periodicity. It should be noted that the effect of velocity smoothing function is neglected from the central part of the image domain as $L \gg \delta$. Once the image vortex contribution is added, steps 4 and 5 are carried out as indicated in Sec. II.

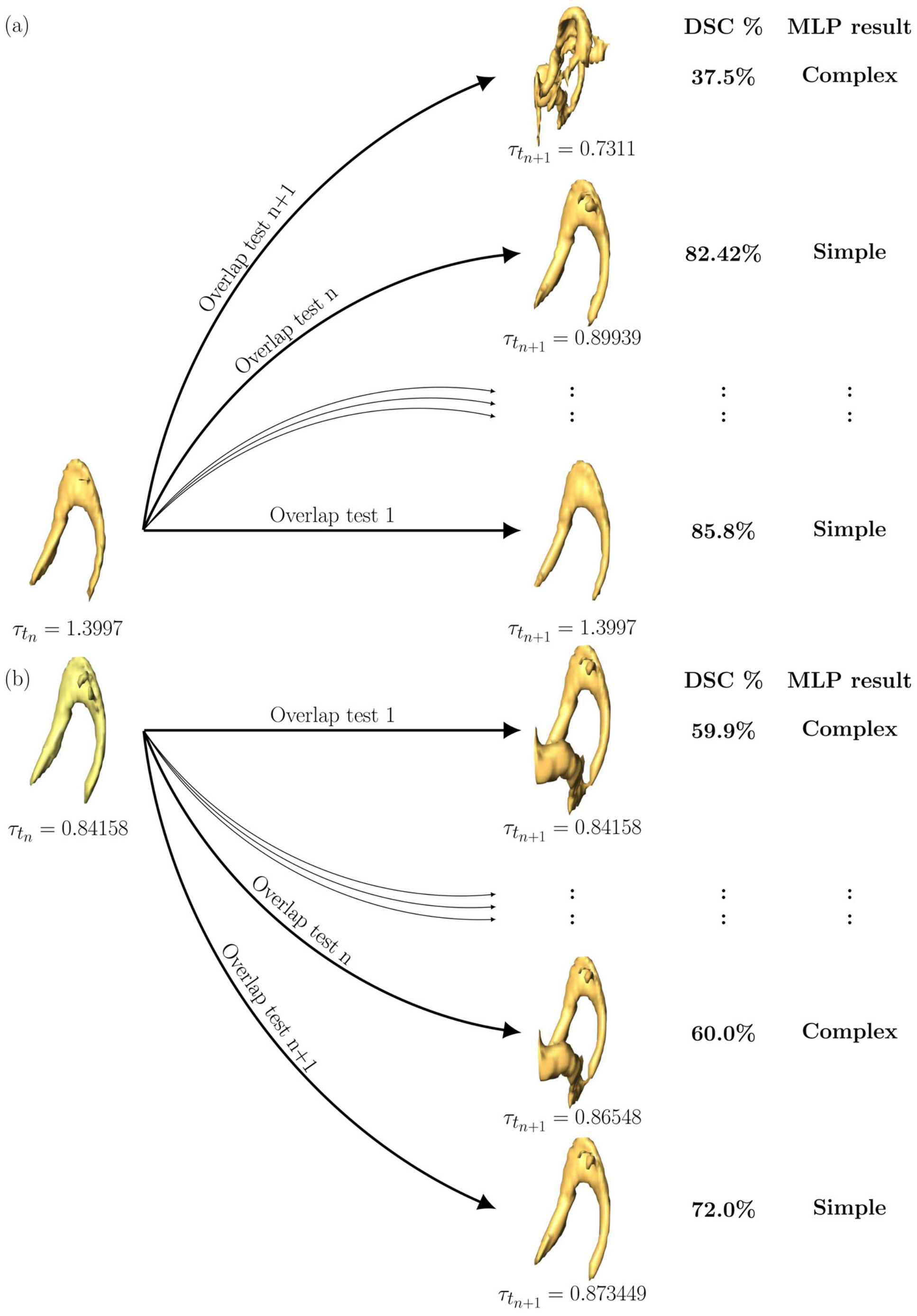

FIG. 24. The process of selecting an optimum threshold for a subsequent time step with MLPT is shown here. The structure is freely allowed to (a) grow and (b) shrink in time with decreasing and increasing the thresholds, respectively.

We will use initial condition R_3 (see Table IV) to test the effect of image vortices at two initial heights $y^+_{\text{initial}} = 15, 30$. The image vortices are placed at $y^+_{\text{initial}} = -15, -30$, respectively. Each filament and its image vortex are represented with 600 nodes. Since twice the number of nodes is used in the calculation when image vortices are present, consequently the calculation time is also doubled. The temporal development of these filaments is shown in Fig. 25. In agreement with the findings reported in Moin *et al.*,[53] the image vortices appear to enhance the streamwise advection while actively pushing the filament away from the wall. This effect is clearly visible for the filament at $y^+_{\text{initial}} = 15$. In accordance with our expectations, if the total velocity, i.e., the sum of self-induced velocity and the

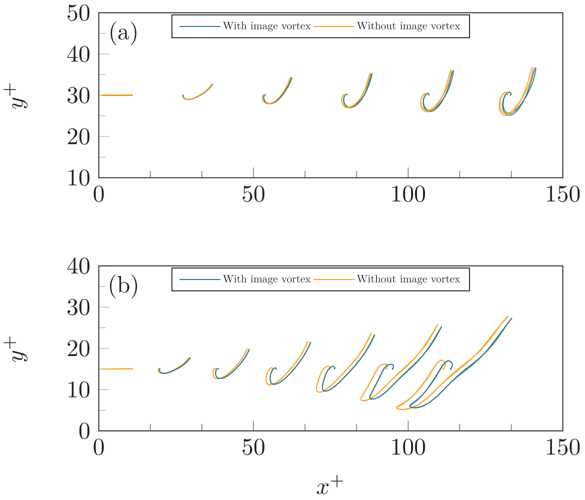

FIG. 25. Evolution of a hairpin filament at two different heights (a) $y^+ = 30$ and (b) $y^+ = 15$ are shown both with and without an image vortex.

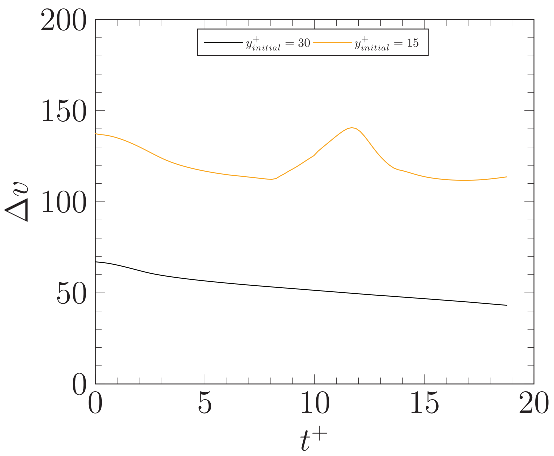

FIG. 26. Time history of the difference between the total velocity with and without an image vortex at two different heights as depicted in Fig. 25.

background flow velocity is summed up for all nodes along the filament, the difference in velocity when an image vortex is present and absent reduces with increasing height (see Fig. 26).

APPENDIX F: THE COMPLETE ASYMPTOTIC ANALYSIS FOR WEAKLY BOUYANT VORTEX FILAMENTS IN THE BOUSSINESQ REGIME

1. The outer solution

The velocity at any point is composed of a velocity $\mathbf{Q}_f$ due to the self-induced motion of the vortex filament and a velocity $\mathbf{Q}_2$ given by the background flow field. $\mathbf{Q}_f$, given by Eq. (33), at any point is not on the vortex centerline. The vortex filament is assumed to be given parametrically by $\mathbf{X}(s,t)$, where s is the arc length along the filament, and t is the time. The position vector of any point $\mathbf{P}$ in curvilinear coordinates can be associated with $\mathbf{X}(s,t)$ by the following equation:

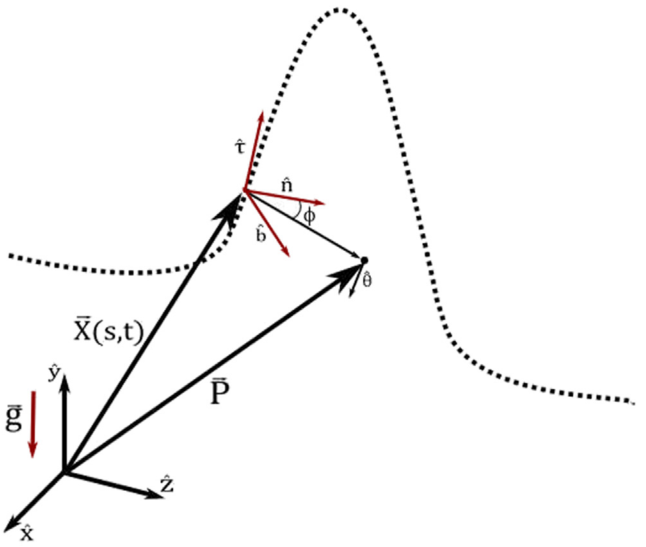

FIG. 27. A sketch of the coordinate system with the dashed line denoting the hairpin shaped vortex filament.

$$\mathbf{P}(x,y,z) = \mathbf{X}(s,t) + r\hat{\mathbf{r}}. \tag{F1}$$

Here, r denotes the distance from the point $\mathbf{P}$ to the filament X, and $\hat{r}$ is the radial unit vector for curvilinear coordinates. The coordinate system is illustrated in Fig. 27. A careful expansion of the integrand in the Biot–Savart formula leads to an expression for the behavior of $\mathbf{Q}_f$ as the radial distance to the filament goes to zero

$$\mathbf{Q}_1(P,t) = \frac{\Gamma}{2\pi r}\hat{\theta} + \frac{\Gamma}{4\pi R}\left[\ln\left(\frac{R}{r}\right)\right]\hat{b} + \frac{\Gamma}{4\pi R}(\cos\phi)\hat{\theta} + \mathbf{Q}_f, \tag{F2}$$

where $\hat{\theta}$ is the unit circumferential vector, and $\hat{b}$ is the unit binormal vector, associated with the point s on the vortex filament $\mathbf{X}(s,t)$. $R = R(s,t)$ is the local radius of curvature, and Γ is the circulation of the filament. The vector $\mathbf{Q}_f$ is a part of the Biot–Savart integral, which has a limit as $r \to 0$. Equation (34) cannot, however, yield the velocity on the vortex filament as the right-hand side diverges as $r \to 0$. To overcome this problem, Callegari and Ting[31] employed a matched asymptotic expansion, where the outer solution, given by Eq. (34), was matched with an inner solution derived from the Navier–Stokes equations with suitable boundary conditions. In the next subsection, we will extend their analysis to include weak gravitational effects.

2. The inner solution

The fluid velocity $v(x,t)$ is described relatively to the moving filament by introducing a relative velocity $\mathbf{V}$

$$v(x,t) = \dot{\mathbf{X}}(s,t) + \mathbf{V}(t,r,\theta,s). \tag{F3}$$

The dimensionless incompressible Navier–Stokes equation in curvilinear coordinates is

$$\ddot{\mathbf{X}}+\left(\frac{w}{h_3}-\frac{r}{h_3}\hat{r}_t\cdot\hat{\tau}\right)\dot{\mathbf{X}}_s+\frac{d\mathbf{V}}{dt} = -\frac{\nabla P}{\rho}+\frac{1}{\mathrm{Re}}\left(\frac{1}{\rho h_3}\left(\frac{1}{h_3}\dot{\mathbf{X}}_s\right)_s+\frac{1}{\rho}\Delta\mathbf{V}\right)+\frac{1}{\mathrm{Fr}^2}\hat{\mathbf{g}}, \tag{F4}$$

where

$$h_3=\sigma[1-\kappa r\cos(\theta+\theta_0)]=\sigma[1-\kappa r\cos\phi] \tag{F5}$$

is the tangential stretching parameter, Re = Reynolds number, Fr = Froude number, P = pressure, and $\sigma=|\mathbf{X}_s|$. The density ρ is assumed to have a fixed part and a variable part, which is dependent exclusively on temperature and not on the pressure. The variable part is assumed to be small. The continuity equation for an incompressible fluid in curvilinear coordinates is

$$\left[(\bar{r}h_3u)_{\bar{r}}+(h_3v)_\theta+r\left(w_s+\dot{\mathbf{X}}_s\cdot\hat{\tau}\right)\right]=0. \tag{F6}$$

We introduce stretched radial coordinates

$$\bar{r}=r/\varepsilon,\quad \varepsilon=(\nu/\Gamma)^{1/2} \tag{F7}$$

with

$$(\nu/\Gamma)^{1/2}=\mathrm{Re}^{-1/2}=\bar{\nu}^{1/2}\varepsilon \tag{F8}$$

and expand the dynamical variables in terms of ε as follows:

$$u(\bar{r},\theta,s,t;\varepsilon)=u^{(1)}(\bar{r},\theta,s,t)+\varepsilon u^{(2)}(\bar{r},\theta,s,t)+\cdots\quad, \tag{F9a}$$

$$v(\bar{r},\theta,s,t;\varepsilon)=\varepsilon^{-1}v^{(0)}(\bar{r},\theta,s,t)+v^{(1)}(\bar{r},\theta,s,t)+\cdots\quad, \tag{F9b}$$

$$w(\bar{r},\theta,s,t;\varepsilon)=\varepsilon^{-1}w^{(0)}(\bar{r},\theta,s,t)+w^{(1)}(\bar{r},\theta,s,t)+\cdots\quad, \tag{F9c}$$

$$\mathbf{X}(s,t;\varepsilon)=\mathbf{X}^{(0)}(s,t)+\varepsilon\mathbf{X}^{(1)}(s,t)+\cdots\quad. \tag{F9d}$$

Here, u, v, and w denote the radial, polar, and tangential components of the velocity vector $\mathbf{V}$, respectively, and ν is the kinematic viscosity. In order to obtain non-trivial velocities $v^{(0)}$ and $w^{(0)}$, the following is required:

$$P(\bar{r},\theta,s,t;\varepsilon)=\varepsilon^{-2}P^{(0)}(\bar{r},\theta,s,t)+\varepsilon^{-1}P^{(1)}(\bar{r},\theta,s,t)+\cdots \tag{F10}$$

along with

$$\dot{\mathbf{X}}\cdot\hat{\tau}=0 \tag{F11}$$

so that the filament core forms a material curve. Through the Serret–Frenet formulas, the geometric parameters σ, κ, and h are functions of $\mathbf{X}(s,t)$ and are expanded as follows:

$$\sigma=\sigma^{(0)}+\varepsilon\sigma^{(1)}+\cdots=|\mathbf{X}_s^{(0)}|+\frac{\varepsilon\mathbf{X}_s^{(0)}\cdot\mathbf{X}_s^{(1)}}{|\mathbf{X}_s^{(0)}|}+\cdots\quad, \tag{F12a}$$

$$\kappa=\kappa^{(0)}+\varepsilon\kappa^{(1)}+\cdots, \tag{F12b}$$

$$h_3=h_3^{(0)}+\varepsilon h_3^{(1)}+\cdots=\sigma^{(0)}+\varepsilon\left[\sigma^{(1)}-\sigma^{(0)}\kappa^{(0)}\bar{r}\cos\varphi^{(0)}\right]. \tag{F12c}$$

Given our choice of ε, the viscosity terms will only enter at higher order. One can show that the term

$$\left(\frac{1}{\rho h_3}\left(\frac{1}{h_3}\dot{\mathbf{X}}_s\right)_s\right) \tag{F13}$$

is at least $\mathcal{O}(\varepsilon)$, so this term only enters much later in the expansion. The Froude number will be assumed to be small such that the gravity term only appears in the second order equations. Specifically, we assume that $\mathrm{Fr}=\bar{\lambda}\sqrt{\varepsilon}$. In the Boussinesq approximation, the density variation only enters in the buoyancy term, $\rho\mathbf{g}$, and can be neglected in the rest of the equation. This yields

$$\rho_0\left(\ddot{\mathbf{X}}+\frac{1}{h_3}(w-r\hat{\mathbf{r}}_t\cdot\hat{\boldsymbol{\tau}})\dot{\mathbf{X}}_s+\frac{d\mathbf{V}}{dt}\right) = -\nabla P+\frac{1}{\mathrm{Re}}\left(\frac{1}{h_3}\left(\frac{1}{h_3}\dot{\mathbf{X}}_s\right)_s+\Delta\mathbf{V}\right)+\rho\frac{1}{\mathrm{Fr}^2}\hat{\mathbf{g}}, \tag{F14}$$

where the temperature and pressure dependent density, ρ, have been replaced by a constant density ρ_0, except in the buoyancy term, which is written as

$$(\rho_0+\Delta\rho)g, \tag{F15}$$

where $\Delta\rho=\rho-\rho_0$ represents the density variation with respect to the reference density ρ_0. This can be further rewritten noting that the variation in density will be exclusively due to temperature variations and not pressure variations, which yields

$$(\rho-\rho_0)g=-\rho_0\beta(T-T_0)g, \tag{F16}$$

where β is the coefficient of thermal expansion. For ideal gases, $\beta=1/T_0$. We expand the perturbation temperature $\tilde{T}=T-T_0$ in an asymptotic series as follows:

$$\tilde{T}(\bar{r},\theta,s,t;\varepsilon)=\tilde{T}^{(0)}(\bar{r},\theta,s,t)+\varepsilon\tilde{T}^{(1)}(\bar{r},\theta,s,t)+\cdots. \tag{F17}$$

Since we have introduced a density variation to the flow, we also need an energy equation to close the system. The energy equation for a Boussinesq fluid in curvilinear, compressed coordinates, in terms of the temperature, T, is

$$\frac{\partial T}{\partial t}+\left(\mathbf{V}-\varepsilon\bar{r}\frac{\partial\hat{\mathbf{r}}}{\partial t}\right)\cdot\nabla T=\frac{1}{\mathrm{Re\,Pr}}\Delta T, \tag{F18}$$

where Pr is the Prandtl number. Here, we have used the formula (B12) for the material derivative provided in Callegari and Ting[31] Appendix B. We make the assumption that $\mathrm{Pr}=\mathcal{O}(1)=\bar{\mu}$. Hence, the leading order temperature equation is $\mathcal{O}(\varepsilon^{-2})$, yielding

$$T_\theta^{(0)}=0. \tag{F19}$$

The first order, or $\mathcal{O}(\varepsilon^{-1})$, equation is

$$\frac{v^{(0)}}{\bar{r}}T_\theta^{(1)}+u^{(1)}T_{\bar{r}}^{(0)}+\frac{w^{(0)}}{\sigma^{(0)}}T_s^{(0)}=0. \tag{F20}$$

Taking the average of F20 with respect to θ yields the symmetric first order equation

$$u_c^{(1)}T_{\bar{r}}^{(0)}+\frac{w^{(0)}}{\sigma^{(0)}}T_s^{(0)}=0, \tag{F21}$$

where the subscript c denotes the symmetric part of $u^{(1)}$.

In what follows, we shall assume that $\mathrm{Pr} = \mathcal{O}(1) = \bar{\mu}$. By inserting the asymptotic expansion, Eqs. (F9a)–(F9d) into Eqs. (F14) and (F6), one gets a hierarchy of equations based on the order of ε. From the leading and first order equations, one can derive an expression for the core constant $C(t)$, which appears in the filament velocity equation. Since the gravity term only appears in the second order equations, the derivation follows that of Callegari and Ting exactly. Hence, we will not repeat it in detail here, but merely state the main results. We refer the reader to Callegari and Ting,[31] or equivalently, Klein and Knio,[32] for the complete derivation.

First, the leading order equations imply that the leading order variables, $v^{(0)}$, $w^{(0)}$, $P^{(0)}$, and $\tilde{T}^{(0)}$, are all θ-independent. Second, since the leading order term in the circumferential velocity term of the outer flow is independent of the axial locations, we will assume that the leading order variables are also independent of the axial coordinate s. With these simplifications, the first order momentum equations can be solved by introduction of an appropriate stream function and further decomposition into symmetric and anti-symmetric parts, finally yielding the following expression for the core constant:

$$C(t) = 2\left[\frac{1}{2}\lim_{\bar{r}\to\infty}\left(\frac{4\pi^2}{\Gamma^2}\int_0^{\bar{r}}\xi\left(v^{(0)}\right)^2 d\xi - \ln\bar{r}\right) - \frac{1}{4} - \frac{4\pi^2}{\Gamma^2}\int_0^{\bar{r}}\xi\left(w^{(0)}\right)^2 d\xi\right]. \tag{F22}$$

By matching the inner solution with the outer solution, one obtains the following equation for the binormal and normal components of the filament velocity:

$$\hat{b}\cdot\dot{X}^{(0)} = \hat{b}\cdot Q_0 + \kappa^{(0)}\frac{\Gamma}{4\pi}\left(\ln\frac{R^{(0)}}{\varepsilon} + C(t)\right), \tag{F23a}$$

$$\hat{n}\cdot\dot{X}^{(0)} = \hat{n}\cdot Q_0, \tag{F23b}$$

where $R^{(0)} = 1/\kappa^{(0)}$ is the leading term of the radius of curvature of the reference line, and $C(t)$ is given by Eq. (36). Thus, we have arrived at an equation for the evolution of the filament, which depends on the leading order velocity components $v^{(0)}$ and $w^{(0)}$. The compatibility conditions, which determine the leading order velocity components, are derived from the second order momentum and continuity equations. It is here that we will see a deviation from the derivation done by Callegari and Ting, as we have the appearance of buoyancy terms in the momentum equations.

3. The compatibility conditions

The second order momentum equation in the circumferential direction is

$$\begin{aligned}
&v_t^{(0)} + w^{(0)}\hat{\tau}_t\cdot\hat{\theta} + u^{(1)}v_{\bar{r}}^{(1)} + \frac{v^{(1)}v_\theta^{(1)}}{\bar{r}} + \frac{v^{(0)}v_\theta^{(2)}}{\bar{r}} + \frac{v^{(0)}u^{(2)}}{\bar{r}}\\
&\quad + \frac{v^{(1)}u^{(1)}}{\bar{r}} + \frac{w^{(0)}v_s^{(1)}}{\sigma^{(0)}} - 2w^{(0)}w^{(1)}\kappa^{(0)}\sin\varphi^{(0)}\\
&\quad - \left(w^{(0)}\right)^{(2)}\left(\frac{\kappa\sigma\sin\varphi}{h_3}\right)^{(1)} + \frac{\theta^{(0)}\cdot\dot{X}_s^{(0)}w^{(0)}}{\sigma^{(0)}} + u^{(2)}v_{\bar{r}}^{(0)}\\
&\quad = -\frac{1}{\bar{r}}\frac{P_\theta^{(2)}}{\rho_0} + \frac{\bar{\nu}}{\bar{r}}\left(\bar{r}v_{\bar{r}}^{(0)}\right)_{\bar{r}} - \frac{\bar{\nu}v^{(0)}}{\bar{r}^2} + \alpha g\tilde{T}^{(0)}\hat{\mathbf{y}}\cdot\hat{\boldsymbol{\theta}},
\end{aligned}$$

where $-\hat{\mathbf{y}}g = \hat{\mathbf{g}}$ denotes the acceleration due to gravity. In addition, we have defined $\alpha = \beta\bar{\lambda}^{-2}$, where the factor of $\bar{\lambda}^{-2}$ comes from the definition of the Froude number. Upon averaging with respect to θ, we get

$$\begin{aligned}
v_t^{(0)} - \bar{\nu}\left[\frac{1}{\bar{r}}\left(\bar{r}v_{\bar{r}}^{(0)}\right)_{\bar{r}} - \frac{v^{(0)}}{\bar{r}^2}\right] &= -\zeta^{(0)}\langle u^{(2)}\rangle\\
&\quad - \frac{1}{\bar{r}}\langle u^{(1)}\left(\bar{r}v^{(1)}\right)_{\bar{r}}\rangle - \frac{w^{(0)}}{\sigma^{(0)}}\langle v_s^{(1)}\rangle\\
&\quad + 2\kappa^{(0)}w^{(0)}\langle w^{(1)}\sin\varphi^{(0)}\rangle,
\end{aligned} \tag{F24}$$

where we have used that $\hat{\boldsymbol{\theta}} = \hat{\mathbf{b}}\cos\varphi^{(0)} - \hat{\mathbf{n}}\sin\varphi^{(0)}$, which in turn implies that

$$\langle\tilde{T}^{(0)}\hat{\mathbf{y}}\cdot\hat{\boldsymbol{\theta}}\rangle = \hat{\mathbf{y}}\cdot\hat{\mathbf{b}}\langle\tilde{T}^{(0)}\cos\varphi^{(0)}\rangle - \hat{\mathbf{y}}\cdot\hat{\mathbf{n}}\langle\tilde{T}^{(0)}\sin\varphi^{(0)}\rangle = 0. \tag{F25}$$

From this, we anticipate that the evolution equation for $v^{(0)}$, derived from Eq. (F24), will not contain any contribution from the gravity term. The second order momentum equation in the tangential direction is

$$\begin{aligned}
&w_t^{(0)} + v^{(0)}\hat{\boldsymbol{\theta}}_t^{(0)}\cdot\hat{\boldsymbol{\tau}} + u^{(2)}w_{\bar{r}}^{(0)} + \frac{w_\theta^{(1)}v^{(1)}}{\bar{r}} + u^{(1)}w_{\bar{r}}^{(1)} + \frac{w_\theta^{(2)}v^{(0)}}{\bar{r}}\\
&\quad + \frac{w^{(0)}w_s^{(1)}}{\sigma^{(0)}} + w^{(1)}v^{(0)}\kappa^{(0)}\sin\varphi^{(0)} + w^{(0)}v^{(1)}\kappa^{(0)}\sin\varphi^{(0)}\\
&\quad - w^{(0)}u^{(1)}\kappa^{(0)}\cos\varphi^{(0)} + w^{(0)}v^{(0)}\left(\frac{\kappa\sigma\sin\varphi}{h_3}\right)^{(1)} + \hat{\boldsymbol{\tau}}\cdot\frac{w^{(0)}}{\sigma^{(0)}}\dot{\mathbf{X}}_s^{(0)}\\
&\quad = -\frac{1}{\sigma^{(0)}}\frac{P_s^{(1)}}{\rho_0} + \frac{\bar{\nu}}{\bar{r}}\left(\bar{r}w_{\bar{r}}^{(0)}\right)_{\bar{r}} + \alpha g\tilde{T}^{(0)}\hat{\mathbf{y}}\cdot\hat{\boldsymbol{\tau}},
\end{aligned} \tag{F26}$$

which, upon averaging with respect to θ, becomes

$$\begin{aligned}
w_t^{(0)} - \frac{\bar{\nu}}{\bar{r}}\left(\bar{r}w_{\bar{r}}^{(0)}\right)_{\bar{r}} &= -w_{\bar{r}}^{(0)}\langle u^{(2)}\rangle - \langle u^{(1)}w_{\bar{r}}^{(1)}\rangle\\
&\quad - \frac{1}{\bar{r}}\langle v^{(1)}w_\theta^{(1)}\rangle - \frac{w^{(0)}}{\sigma^{(0)}}\upsilon\\
&\quad - w^{(0)}\kappa^{(0)}\langle v^{(1)}\sin\varphi - u^{(1)}\cos\varphi^{(0)}\rangle\\
&\quad - v^{(0)}\kappa^{(0)}\langle w^{(1)}\sin\varphi^{(0)}\rangle - \frac{\langle P_s^{(1)}\rangle}{\rho_0\,\sigma^{(0)}} + \alpha g\tilde{T}^{(0)}\hat{\mathbf{y}}\cdot\hat{\boldsymbol{\tau}},
\end{aligned} \tag{F27}$$

where we for the sake of convenience have defined

$$\upsilon = \langle w_s^{(1)}\rangle + \dot{\mathbf{X}}_s^{(0)}\cdot\hat{\boldsymbol{\tau}^{(0)}}. \tag{F28}$$

Through application of the θ-averaged second order continuity equations and first order momentum equation, this can be rewritten to yield

$$\begin{aligned}
\sigma^{(0)}F_1(\bar{r},t) &= \frac{1}{\bar{r}}w_{\bar{r}}^{(0)}\int_0^{\bar{r}}\varrho\upsilon\,d\varrho - w^{(0)}\upsilon - \frac{1}{\rho_0}\langle P_s^{(1)}\rangle\\
&\quad + \sigma^{(0)}\alpha g\hat{\mathbf{y}}\cdot\hat{\boldsymbol{\tau}}\tilde{T}^{(0)},
\end{aligned} \tag{F29}$$

where

$$F_1(\bar{r},t) = w_t^{(0)} - \frac{\bar{\nu}}{\bar{r}}\left(\bar{r}w_{\bar{r}}^{(0)}\right)_{\bar{r}}. \tag{F30}$$

Except for the added buoyancy term (the last term on the r.h.s.), Eq. (F29) is the same as in Callegari and Ting.[31]

Furthermore, we note that $\dot{\mathbf{X}}_s \cdot \hat{\boldsymbol{\tau}} = \dot{\sigma}$ and so $\upsilon = \langle w_s^{(1)} \rangle + \dot{\sigma}$. If we define $\tilde{S}$ such that $\sigma = \tilde{S}_s$, we have $\tilde{S}(s,t) = \int_0^s \sigma(s',t)ds'$ and $\dot{\sigma} = \tilde{S}_{st}$. Similarly, Eq. (F24) can be reformulated as

$$\sigma^{(0)} F_2(\bar{r},t) = -w^{(0)} \langle v_s^{(1)} \rangle + \frac{\zeta^{(0)}}{\bar{r}} \int_0^{\bar{r}} \varrho \upsilon \, d\varrho, \tag{F31}$$

where

$$F_2(\bar{r},t) = v_t^{(0)} - \bar{\nu} \left[\frac{1}{\bar{r}} \left(\bar{r} v_{\bar{r}}^{(0)} \right)_{\bar{r}} - \frac{v^{(0)}}{\bar{r}^2} \right]. \tag{F32}$$

Note that the functions $F_1(\bar{r},t)$ and $F_2(\bar{r},t)$, appearing in Eqs. (F29) and (F31), are independent of s, and that $\sigma^{(0)} = \tilde{S}_s^{(0)}$, where $\tilde{S}^{(0)}(s,t)$ is the leading term in the expansion for the arc length at time t. Furthermore,

$$\dot{\mathbf{X}}_s^{(0)} \cdot \hat{\boldsymbol{\tau}} = \left(\mathbf{X}_s^{(0)} \cdot \hat{\boldsymbol{\tau}} \right)_t = \tilde{S}_{st}^{(0)}. \tag{F33}$$

Thus, integrating (F28) and (F31) over s yields

$$\begin{aligned} F_1(\bar{r},t) S^{(0)}(t) = {} & \frac{1}{2} \bar{r}^3 \left(\frac{w^{(0)}}{\bar{r}^2} \right)_{\bar{r}} \dot{S}^{(0)}(t) - w^{(0)} \int_0^{S_0} \langle w_{s'}^{(1)} \rangle ds' \\ & - \frac{1}{\rho_0} \int_0^{S_0} \langle P_{s'}^{(1)} \rangle ds' \\ & + \alpha g \int_0^{S_0} \hat{\mathbf{y}} \cdot \hat{\boldsymbol{\tau}} \sigma^{(0)} \tilde{T}^{(0)} ds', \end{aligned} \tag{F34}$$

$$\begin{aligned} F_2(\bar{r},t) S^{(0)}(t) = {} & \frac{1}{2} \frac{\left(\bar{r} v^{(0)} \right)_{\bar{r}}}{\bar{r}} \dot{S}^{(0)}(t) \\ & - w^{(0)} \int_0^{S_0} \langle v_{s'}^{(1)} \rangle ds' \\ & + \frac{\zeta^{(0)}}{\bar{r}} \int_0^{S_0} \rho \Gamma \langle w_{s'}^{(1)} \rangle ds'. \end{aligned} \tag{F35}$$

For a closed vortex, the integral over s of $\langle w_s^{(1)} \rangle$, $\langle v_s^{(1)} \rangle$ and $\langle P_s^{(1)} \rangle$ all vanish. This also holds true for open filaments, provided it is periodic in some horizontal direction, as was assumed in Secs. II–IV, such that $w^{(1)}(s = \text{start}) = w^{(1)}(s = \text{end})$. In such cases, we get

$$\begin{aligned} F_1(\bar{r},t) S^{(0)}(t) = {} & \frac{1}{2} \bar{r}^3 \left(\frac{w^{(0)}}{\bar{r}^2} \right)_{\bar{r}} \dot{S}^{(0)}(t) \\ & + \alpha g \int_0^{S_0} \hat{\mathbf{y}} \cdot \hat{\boldsymbol{\tau}} \sigma^{(0)} \tilde{T}^{(0)} ds, \end{aligned} \tag{F36}$$

$$F_2(\bar{r},t) S^{(0)}(t) = \frac{1}{2} \frac{\left(\bar{r} v^{(0)} \right)_{\bar{r}}}{\bar{r}} \dot{S}^{(0)}(t). \tag{F37}$$

Since we have assumed that all the leading order field components are independent of s, we can write

$$\int_0^{S_0} \hat{\mathbf{y}} \cdot \hat{\boldsymbol{\tau}} \sigma^{(0)} \tilde{T}^{(0)} ds = \tilde{T}^{(0)}(\bar{r},t) \int_0^{S_0} \hat{\mathbf{y}} \cdot \hat{\boldsymbol{\tau}} \sigma^{(0)} ds. \tag{F38}$$

The integrand can be written as

$$\hat{\mathbf{y}} \cdot (d\mathbf{X}), \tag{F39}$$

thus implying that

$$\int_0^{S_0} \hat{\mathbf{y}} \cdot \hat{\boldsymbol{\tau}} \sigma^{(0)} ds = \int_0^{S_0} \hat{\mathbf{y}} \cdot (d\mathbf{X}) = \hat{\mathbf{y}} \cdot (\mathbf{X}(S_0) - \mathbf{X}(0)). \tag{F40}$$

For the sake of completeness, we include the derivation of an equation for the temporal evolution of $\tilde{T}^{(0)}$. This equation is derived from the second order temperature equation

$$\begin{aligned} T_t^{(0)} + {} & \frac{1}{\bar{r}} T_\theta^{(2)} v^{(0)} + \frac{w^{(0)}}{\sigma^{(0)}} T_s^{(1)} + u^{(1)} T_{\bar{r}}^{(1)} + \frac{v^{(1)}}{\bar{r}} T_\theta^{(1)} \\ & + u^{(2)} T_{\bar{r}}^{(0)} - \bar{r} \frac{\partial \hat{\mathbf{r}}}{\partial t} \cdot \hat{\mathbf{r}} T_{\bar{r}}^{(0)} = \frac{\bar{\nu}}{\bar{r} \bar{\mu}} \left(\bar{r} T_{\bar{r}}^{(0)} \right)_{\bar{r}}. \end{aligned} \tag{F41}$$

Taking the average of this equation w.r.t. θ yields

$$\begin{aligned} T_t^{(0)} + {} & \frac{w^{(0)}}{\sigma^{(0)}} T_s^{(1)} + \langle u^{(1)} T_{\bar{r}}^{(1)} \rangle \\ & + \frac{1}{\bar{r}} \langle v^{(1)} T_\theta^{(1)} \rangle + \langle u^{(2)} \rangle T_{\bar{r}}^{(0)} = \frac{\bar{\nu}}{\bar{r} \bar{\mu}} \left(\bar{r} T_{\bar{r}}^{(0)} \right)_{\bar{r}}, \end{aligned} \tag{F42}$$

which, through application of the first order continuity equation, can be written as

$$\begin{aligned} T_t^{(0)} + {} & \frac{w^{(0)}}{\sigma^{(0)}} T_s^{(1)} - \frac{T_{\bar{r}}^{(0)}}{\bar{r} \sigma^{(0)}} \int_0^{\bar{r}} \varrho \left[\langle w_s^{(1)} \rangle + \langle \dot{\mathbf{X}}_s^{(0)} \cdot \hat{\boldsymbol{\tau}} \rangle \right] d\varrho \\ & = \frac{\bar{\nu}}{\bar{r} \bar{\mu}} \left(\bar{r} T_{\bar{r}}^{(0)} \right)_{\bar{r}}. \end{aligned} \tag{F43}$$

Here, we have used that

$$\langle \left(T^{(1)} v^{(1)} \right)_\theta \rangle = \langle T^{(1)} u^{(1)} \rangle = 0, \tag{F44}$$

which holds for flows in which the leading order field components are axially independent.[37] Integrating Eq. (F43) w.r.t. s, using the symmetry condition, yields

$$T_t^{(0)} S^{(0)} - \frac{1}{2} T_{\bar{r}}^{(0)} \bar{r} \dot{S}^{(0)}(t) - \frac{\bar{\nu}}{\bar{r} \bar{\mu}} \left(\bar{r} T_{\bar{r}}^{(0)} \right)_{\bar{r}} S^{(0)} = 0. \tag{F45}$$

Within the Boussinesq approximation, we require that leading order temperature difference, $\tilde{T}^{(0)}$, decays exponentially as $\bar{r}$ becomes large, or in other words

$$\tilde{T}^{(0)} = o(\bar{r}^{-n}) \quad \text{for all } n \text{ as } \bar{r} \to \infty. \tag{F46}$$

The exponential decay of $\tilde{T}^{(0)}$ means that an analytic solution to Eq. (F45) can be obtained, for large time t, in terms of Laguerre polynomials. We do not include the calculation here, but refer to Callegari and Ting[31] on how to approach this problem.

Thus, for non-closed filaments lacking horizontal symmetry, one would need to combine Eqs. (F29), (F31), and (F45) together with equations for the first order pressure and axial velocity component to arrive at an expression for the core constant. The equations for the first order pressure and axial velocity component are not included here, but can in principle be derived from higher order equations following standard asymptotic techniques. If these equations are solved analytically, they will yield expressions for the leading order velocity field components needed to determine the core constant $C(t)$. This new core constant can be implemented directly in the M1 KK method to observe the effect of gravity on the motion of hairpin filaments. However, this is beyond the current scope of the paper and will be pursued in a future work.

REFERENCES

[1] M. Head and P. Bandyopadhyay, "New aspects of turbulent boundary-layer structure," J. Fluid Mech. **107**, 297–338 (1981).

[2] M. Acarlar and C. Smith, "A study of hairpin vortices in a laminar boundary layer—Part 1: Hairpin vortices generated by a hemisphere protuberance," J. Fluid Mech. **175**, 1–41 (1987).

[3] M. Acarlar and C. Smith, "A study of hairpin vortices in a laminar boundary layer—Part 2: Hairpin vortices generated by fluid injection," J. Fluid Mech. **175**, 43–83 (1987).

[4] R. J. Adrian, C. D. Meinhart, and C. D. Tomkins, "Vortex organization in the outer region of the turbulent boundary layer," J. Fluid Mech. **422**, 1–54 (2000).

[5] S. K. Robinson, "The kinematics of turbulent boundary layer structure," Ph.D. thesis (Stanford University, 1991).

[6] R. J. Adrian, "Hairpin vortex organization in wall turbulence," Phys. Fluids **19**, 041301 (2007).

[7] J. Zhou, R. J. Adrian, S. Balachandar, and T. Kendall, "Mechanisms for generating coherent packets of hairpin vortices in channel flow," J. Fluid Mech. **387**, 353–396 (1999).

[8] A. Harikrishnan, C. Ansorge, R. Klein, and N. Vercauteren, "Geometry and organization of coherent structures in stably stratified atmospheric boundary layers," arXiv:2110.02253 (2021).

[9] C. Ansorge and J. P. Mellado, "Global intermittency and collapsing turbulence in the stratified planetary boundary layer," Boundary-Layer Meteorol. **153**, 89–116 (2014).

[10] C. Ansorge and J. P. Mellado, "Analyses of external and global intermittency in the logarithmic layer of Ekman flow," J. Fluid Mech. **805**, 611–635 (2016).

[11] C. Ansorge, *Analyses of Turbulence in the Neutrally and Stably Stratified Planetary Boundary Layer* (Springer, 2016).

[12] L. Mahrt, "Intermittency of atmospheric turbulence," J. Atmos. Sci. **46**, 79–95 (1989).

[13] J. C. Hunt, A. A. Wray, and P. Moin, "Eddies, streams, and convergence zones in turbulent flows," in Studying Turbulence Using Numerical Simulation Databases, 2. Proceedings of the 1988 Summer Program (1988).

[14] A. Harikrishnan, C. Ansorge, R. Klein, and N. Vercauteren, "The curious nature of hairpin vortices. Gallery of Fluid Motion," in 73rd Annual Meeting of the APS Division of Fluid Dynamics (2020).

[15] A. Harikrishnan, C. Ansorge, R. Klein, and N. Vercauteren, "Lagrangian hairpins in atmospheric boundary layers. Gallery of Fluid Motion," in 74th Annual Meeting of the APS Division of Fluid Dynamics (2021).

[16] M. A. Green, C. W. Rowley, and G. Haller, "Detection of Lagrangian coherent structures in three-dimensional turbulence," J. Fluid Mech. **572**, 111–120 (2007).

[17] S. E. Hommema and R. J. Adrian, "Packet structure of surface eddies in the atmospheric boundary layer," Boundary-Layer Meteorol. **106**, 147–170 (2003).

[18] D. Li and E. Bou-Zeid, "Coherent structures and the dissimilarity of turbulent transport of momentum and scalars in the unstable atmospheric surface layer," Boundary-Layer Meteorol. **140**, 243–262 (2011).

[19] M. Heisel, T. Dasari, Y. Liu, J. Hong, F. Coletti, and M. Guala, "The spatial structure of the logarithmic region in very-high-Reynolds-number rough wall turbulent boundary layers," J. Fluid Mech. **857**, 704–747 (2018).

[20] S. Lee, S. I. Gohari, and S. Sarkar, "Direct numerical simulation of stratified Ekman layers over a periodic rough surface," J. Fluid Mech. **902**, A25 (2020).

[21] S. P. Oncley, O. Hartogensis, and C. Tong, "Whirlwinds and hairpins in the atmospheric surface layer," J. Atmos. Sci. **73**, 4927–4943 (2016).

[22] T. Watanabe, J. J. Riley, K. Nagata, K. Matsuda, and R. Onishi, "Hairpin vortices and highly elongated flow structures in a stably stratified shear layer," J. Fluid Mech. **878**, 37–61 (2019).

[23] S. J. Kline, W. C. Reynolds, F. Schraub, and P. Runstadler, "The structure of turbulent boundary layers," J. Fluid Mech. **30**, 741–773 (1967).

[24] E. M. Saiki, C.-H. Moeng, and P. P. Sullivan, "Large-eddy simulation of the stably stratified planetary boundary layer," Boundary-Layer Meteorol. **95**, 1–30 (2000).

[25] M. Jiménez and J. Cuxart, "Large-eddy simulations of the stable boundary layer using the standard Kolmogorov theory: Range of applicability," Boundary-Layer Meteorol. **115**, 241–261 (2005).

[26] I. Marusic, G. J. Kunkel, and F. Porté-Agel, "Experimental study of wall boundary conditions for large-eddy simulation," J. Fluid Mech. **446**, 309–320 (2001).

[27] K. Chauhan, N. Hutchins, J. Monty, and I. Marusic, "Structure inclination angles in the convective atmospheric surface layer," Boundary-layer Meteorol. **147**, 41–50 (2013).

[28] A. Lozano-Durán and J. Jiménez, "Time-resolved evolution of coherent structures in turbulent channels: Characterization of eddies and cascades," J. Fluid Mech. **759**, 432–471 (2014).

[29] T. Hon and J. Walker, "Evolution of hairpin vortices in a shear flow," NASA Technical Memorandum No. 100858 (1988).

[30] A. Leonard, "Computing three-dimensional incompressible flows with vortex elements," Annu. Rev. Fluid Mech. **17**, 523–559 (1985).

[31] A. J. Callegari and L. Ting, "Motion of a curved vortex filament with decaying vortical core and axial velocity," J. Appl. Math. **35**, 148–175 (1978).

[32] R. Klein and O. M. Knio, "Asymptotic vorticity structure and numerical simulation of slender vortex filaments," J. Fluid Mech. **284**, 275 (1995).

[33] F. R. Hama, "Progressive deformation of a curved vortex filament by its own induction," Phys. Fluids **5**, 1156–1162 (1962).

[34] C. Chang and S. G. L. Smith, "The motion of a buoyant vortex filament," J. Fluid Mech. **857**, R1 (2018).

[35] D. W. Moore and P. G. Saffman, "The motion of a vortex filament with axial flow," Philos. Trans. R. Soc. London Ser. A **272**, 403–429 (1972).

[36] J. S. Turner, "Buoyant vortex rings," Proc. R. Soc. Lond. A **239**, 61–75 (1957).

[37] L. Ting, R. Klein, and O. M. Knio, *Vortex Dominated Flows: Analysis and Computation for Multiple Scale Phenomena* (Springer-Verlag, 2007).

[38] O. M. Knio, L. Ting, and R. Klein, "Theory of slender compressible vortex filaments," in *Proceedings of Second MIT Conference on Computational Fluid Dynamics and Solid Mechanics* (Elsevier, 2003), pp. 971–973.

[39] O. M. Knio and R. Klein, "Improved thin-tube models for slender vortex simulations," J. Comput. Phys. **163**, 68–82 (2000).

[40] T.-L. Hon and J. D. A. Walker, "Evolution of hairpin vortices in a shear flow," Comput. Fluids **20**, 343–358 (1991).

[41] R. Arms and F. R. Hama, "Localized-induction concept on a curved vortex and motion of an elliptic vortex ring," Phys. Fluids **8**, 553–559 (1965).

[42] H. Zhou, *Numerical Analysis of Slender Vortex Motion* (University of California, Berkeley, 1996).

[43] D. Margerit, P. Brancher, and A. Giovannini, "Implementation and validation of a slender vortex filament code: Its application to the study of a four-vortex wake model," Int. J. Numer. Methods Fluids **44**, 175–196 (2004).

[44] G. K. Batchelor, *An Introduction to Fluid Dynamics* (Cambridge University Press, 2000).

[45] R. Klein and A. J. Majda, "Self-stretching of a perturbed vortex filament—I: The asymptotic equation for deviations from a straight line," Physica D **49**, 323–352 (1991).

[46] R. Klein and A. J. Majda, "Self-stretching of perturbed vortex filaments—II: Structure of solutions," Physica D **53**, 267–294 (1991).

[47] A. J. Chorin, "Vortex models and boundary layer instability," SIAM J. Sci. Stat. Comput. **1**, 1 (1980).

[48] O. M. Knio and A. F. Ghoniem, "Numerical study of a three-dimensional vortex method," J. Comput. Phys. **86**, 75–106 (1990).

[49] L. Ting and R. Klein, *Viscous Vortical Flows* (Springer, 1991), Vol. 374.

[50] O. M. Knio and A. F. Ghoniem, "Three-dimensional vortex simulation of rollup and entrainment in a shear layer," J. Comput. Phys. **97**, 172–223 (1991).

[51] J. C. Butcher, *Numerical Methods for Ordinary Differential Equations* (John Wiley & Sons, 2016).

[52] E. Hairer, G. Wanner, and S. P. Nørsett, "Runge-Kutta and extrapolation methods," in *Solving Ordinary Differential Equations I: Nonstiff Problems* (Springer, 1993), pp. 129–353.

[53] P. Moin, A. Leonard, and J. Kim, "Evolution of a curved vortex filament into a vortex ring," Phys. Fluids **29**, 955–963 (1986).

[54] C. Fouard, G. Malandain, S. Prohaska, and M. Westerhoff, "Blockwise processing applied to brain microvascular network study," IEEE Trans. Med. Imaging **25**, 1319–1328 (2006).

[55] E. Abbena, S. Salamon, and A. Gray, *Modern Differential Geometry of Curves and Surfaces with Mathematica* (Chapman and Hall/CRC, 2017).

[56] H. Aref and E. P. Flinchem, "Dynamics of a vortex filament in a shear flow," J. Fluid Mech. **148**, 477–497 (1984).

[57] J. Yao and F. Hussain, "On singularity formation via viscous vortex reconnection," J. Fluid Mech. **888**, R2 (2020).

[58] J. Yao and F. Hussain, "Vortex reconnection and turbulence cascade," Annu. Rev. Fluid Mech. **54**, 317–347 (2022).

[59] E. Deusebio, G. Brethouwer, P. Schlatter, and E. Lindborg, "A numerical study of the unstratified and stratified Ekman layer," J. Fluid Mech. **755**, 672–704 (2014).

[60] A. Bußmann, J. Buchmeier, M. Dodd, S. Adami, and I. Bermejo-Moreno, "Tracking and analysis of interfaces and flow structures in multiphase flows," Comput. Fluids **248**, 105665 (2022).

[61] J. von Lindheim, A. Harikrishnan, T. Dörffel, R. Klein, P. Koltai, N. Mikula, A. Müller, P. Névir, G. Pacey, R. Polzin *et al.*, "Definition, detection, and tracking of persistent structures in atmospheric flows," arXiv:2111.13645 (2021).

[62] F. Moisy and J. Jiménez, "Geometry and clustering of intense structures in isotropic turbulence," J. Fluid Mech. **513**, 111–133 (2004).

[63] T. Günther and H. Theisel, "The state of the art in vortex extraction," in *Computer Graphics Forum* (Wiley Online Library, 2018), Vol. 37, pp. 149–173.

[64] J. C. Del Alamo and J. Jimenez, "Linear energy amplification in turbulent channels," J. Fluid Mech. **559**, 205–213 (2006).

[65] L. R. Dice, "Measures of the amount of ecologic association between species," Ecology **26**, 297–302 (1945).

[66] R. Klein, O. M. Knio, and L. Ting, "Representation of core dynamics in slender vortex filament simulations," Phys. Fluids **8**, 2415–2425 (1996).

[67] L. Mahrt, "Stably stratified atmospheric boundary layers," Annu. Rev. Fluid Mech. **46**, 23–45 (2014).